

Spring 2017

Synthesis, Characterization, and Properties of Graphene-Based Hybrids with Cobalt Oxides for Electrochemical Energy Storage and Electrocatalytic Glucose Sensing

Sara C. Botero Carrizosa
Western Kentucky University, Sara.Botero.94@gmail.com

Follow this and additional works at: <http://digitalcommons.wku.edu/theses>

 Part of the [Catalysis and Reaction Engineering Commons](#), [Materials Chemistry Commons](#), and the [Physics Commons](#)

Recommended Citation

Botero Carrizosa, Sara C., "Synthesis, Characterization, and Properties of Graphene-Based Hybrids with Cobalt Oxides for Electrochemical Energy Storage and Electrocatalytic Glucose Sensing" (2017). *Masters Theses & Specialist Projects*. Paper 1941.
<http://digitalcommons.wku.edu/theses/1941>

This Thesis is brought to you for free and open access by TopSCHOLAR®. It has been accepted for inclusion in Masters Theses & Specialist Projects by an authorized administrator of TopSCHOLAR®. For more information, please contact topscholar@wku.edu.

SYNTHESIS, CHARACTERIZATION, AND PROPERTIES OF GRAPHENE-BASED
HYBRIDS WITH COBALT OXIDES FOR ELECTROCHEMICAL ENERGY
STORAGE AND ELECTROCATALYTIC GLUCOSE SENSING

A Thesis
Presented to
The Faculty of the Department of Chemistry
Western Kentucky University
Bowling Green, Kentucky

In Partial Fulfillment
Of the Requirements for the Degree
Master of Science

By
Sara C. Botero Carrizosa

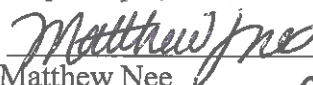
May 2017

SYNTHESIS, CHARACTERIZATION, AND PROPERTIES OF GRAPHENE-BASED
HYBRIDS WITH COBALT OXIDES FOR ELECTROCHEMICAL ENERGY
STORAGE AND ELECTROCATALYTIC GLUCOSE SENSING

Date Recommended 04/18/2017



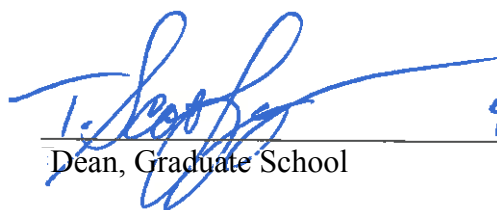
Sanju Gupta, Director of Thesis



Matthew Nee



Darwin Dahl



Dean, Graduate School

4/24/17

Date

ACKNOWLEDGMENTS

I would like to acknowledge Prof. Sanju Gupta (Department of Physics and Astronomy) for all of the guidance she provided on this thesis and my scientific endeavors. I also thank her for the time, effort, and careful considerations she provided to this project without which this would not have been possible.

I would like to thank Drs. Dahl and Nee for serving on my thesis committee and Dr. Burris as Chair of the Department of Chemistry. I also thank all of those who have provided me direct assistance in training of various instruments and data collection for this work: Dr. Jacek Jasinski (Conn Center, University of Louisville), Pauline Norris (Advanced Materials Institute, AMI), Dr. John Andersland (Electron Microscopy), Dr. Quentin Lineberry (Thermal Detection and X-ray Diffraction Labs at AMI), and my laboratory colleagues Carson Price, Benjamin McDonald, Bryce Aberg and Jared Walden for keeping up company and occasional assistance in the laboratory. I would like to thank as well Ms Haley Smith, Department of Chemistry office associate for the administrative support, Ms Haleh Jeddi and Ms Aubrey Penn, as part of the Chemistry JUMP program contemporaries, for their friendship.

Finally, this research project for my thesis was financially supported in parts by NSF KY EPSCoR RSP Grant, WKU Research Foundation RCAP-I internal grant (awarded to Dr. Gupta) and department of chemistry graduate teaching assistantship.

CONTENTS

Chapter 1: Introduction.....	1
1.1 Organization of Thesis.....	1
1.2 Motivation and Background.....	2
1.3 Nanomaterials for Electrochemical Energy Conversion and Storage.....	3
1.3.1 Carbon-based Materials and Graphene.....	3
1.3.2 Other Potential Materials.....	6
1.3.3 Hybrid Nanomaterials	7
1.4 Electrochemical Principles	9
1.4.1 Supercapacitors and Pseudocapacitors.....	10
1.4.2 Rechargeable Secondary Batteries.....	11
1.4.3 Electrocatalysis and Sensing.....	11
1.5 Characterization Techniques.....	13
1.5.1 Electron Microscopy: Surface Morphology and Microscopic Structure.....	13
1.5.2 X-Ray Diffraction and Raman Spectroscopy: Crystal and Lattice Structure.....	14
1.5.3 Electrochemistry and Electrochemical Microscopy.....	15
Chapter 2: Synthesis and Structural Characterization of Graphene-based Hybrids.....	20

2.1 Experimental Synthetic Approaches.....	20
2.1.1 Physical Deposition.....	20
2.2.2 Electrodeposition.....	21
2.2.3 Hydrothermal.....	24
2.3 Results and Discussion.....	25
2.4 Conclusion.....	48
Chapter 3: Electrochemical Properties of Graphene-based Hybrid Nanomaterials	49
3.1 Results and Discussion.....	49
3.2 Conclusion.....	64
Chapter 4: Summary and Future Prospects	66
Appendix A: In Situ Raman Spectroelectrochemistry of Graphene-based Hybrids	68
References	72

LIST OF FIGURES

- Figure 1.** Depiction of the chemical structure of: (a) diamond, (b) graphite, (c) amorphous carbon, (d) fullerene (C₆₀), and (e) SWCNT and MWCNT, (f) graphene; Gr, (g) graphene oxide; GO, and (h) reduced GO; rGO.....4
- Figure 2.** The crystal structure for both CoO (fcc) and Co₃O₄ (cubic spinel)7
- Figure 3.** Schematic illustration of transition metal oxides–carbon-based support interfaces: (a) pristine interface or direct contact; (b) bonding between atoms of transition metal oxide and the defect sites of carbon-based support; (c) noncovalent interactions of functional moieties of carbon-based support with transition metal oxides, and (d) covalent bonding of carbon-based support and transition metal oxide.....8
- Figure 4.** Depiction of the different layers (inner Helmholtz layer- IHP, outer Helmholtz layer-OHP, and diffuser layer) on a EDLC.....9
- Figure 5.** Scheme of an alkaline fuel cell. Adapted from Ref 54.....12
- Figure 6.** (a) Scheme of the micro-electrode arrangement for SECM and illustration of SECM principles when (b) tip is far from the substrate, (c) and (d) tip is near the substrate adopted from Ref. 48.....18
- Figure 7.** Amperometric plots (*i-t* curves) for electrochemical deposition of Co oxide polymorphs (a) Co₃O₄ and (b) CoO and (d) Co nanoparticles alone and on various graphene-supports.....22
- Figure 8.** Illustration of electrochemical deposition through Amperometry mode of cobalt oxide polymorphs on GO, ErGO and MLG with the respective parameters⁶⁸.....23
- Figure 9.** Illustration of hydrothermal synthesis of Co₃O₄ embedded on GO and rGO architectures.....25
- Figure 10.** SEM images of GO and rGO and their hybrids with CoO and Co₃O₄. (Scale bars are shown at the bottom of the images)26
- Figure 11.** TEM images for (a) CoO, Co₃O₄, and GO, (b) representative hybrids Co₃O₄/GO and CoO/GO with corresponding SAED patterns, and (c) the electron tomography three-dimensional images for CoO/GO hybrid is included (Scale bars are shown at the bottom of the images).....27
- Figure 12.** XRD diffractograms for (a) GO and rGO, (b) CoO and Co₃O₄, and (c) their hybrids, peaks of interest for hybrids are marked with their (hkl) index.....29
- Figure 13.** Micro-Raman spectra of (a) GO and rGO, (c) nano-/microscale cobalt oxides

CoO, Co₂O₃, Co₃O₄, and (b, c) their corresponding hybrids.....32

Figure 14. Variation of prominent Raman spectral bands for GO and rGO hybrids with CoO and Co₃O₄ in terms of (a) ω_D , (b) ω_G , (c) I_D/I_G , (d) ω_{2D} , (e) I_{Co}/I_G , (f) I_{2D}/I_G , and (g) ω_{2D} versus ω_G band determining the defect types [*i.e.* residual or neutral versus charged (*p*- or *n*-type)]36

Figure 15. Raman mapping of (a) CoO/rGO and (b) Co₃O₄/rGO in terms of intensity distribution of D, G, 2D and Co bands and their ratio with G band, corresponding optical micrographs, possible surface charge transfer *via* plot of 2D band to G band position for (a) CoO/rGO hybrid. The black regions represent either the substrate (SiO₂) or lower bound as shown with scale bar adjacent.....38

Figure 16. SEM images of (a) CoO and (b) Co₃O₄, ErGO with (c) CoO and (d) Co₃O₄ hybrids, and (e) multilayered graphene on Ni foam and hybrids with (f) CoO, (g) Co₃O₄, and (h) CoNP. (Scale bars are shown at the bottom of the images)41

Figure 17. TEM images for (a) CoO, (b) Co₃O₄, and (c, d) CoNP, (e) ErGO and (f) GO with CoO, (g) ErGO with Co₃O₄.....42

Figure 18. XRD diffractograms with their respective amplifications for (a) Co₃O₄ and corresponding hybrids with graphene based supports on ITO substrate, (b) CoO, CoNP and corresponding hybrids with MLG on Ni foam substrate. The peaks of interest for hybrids are marked with their (hkl) index.....43

Figure 19. Micro-Raman spectra showing characteristic peaks for (a) cobalt oxides and CoNP, ErGO, rGO, and GO hybrids with nano-/microscale (b) CoO and (c) Co₃O₄, and (d) MLG on Ni foam decorated with Co₃O₄, CoNP, and CoO.....44

Figure 20. SEM (a) and TEM (b) images of hydrothermally synthesized GO and rGO with Co₃O₄. (Scale bars are shown at the bottom of the images)46

Figure 21. (a) XRD diffractograms and (b) micro-Raman spectra of GO and rGO hydrothermally synthesized hybrids with Co₃O₄.....47

Figure 22. Cyclic voltammograms for representative (a) CoO (top) and (b) Co₃O₄ (top) with their corresponding ErGO hybrid (bottom) for scan rates 10, 20, 50, 100, 200 mV/s.....50

Figure 23. CV analyses in the form of current as a function of square root of scan rate for (a) CoO/graphene and (b) Co₃O₄/graphene hybrids.....51

Figure 24. CV analyses in terms of gravimetric capacitance as a function of scan rate for (a) CoO/graphene and (b) Co₃O₄/graphene hybrids.....52

Figure 25. Nyquist plots ($-Z''$ vs. Z') for (a) CoO and CoNP and for (b) Co ₃ O ₄ , based hybrids and (c) the Randles' circuit with its corresponding elements.....	53
Figure 26. C _{if} values for (a) CoO and CoNP and (b) Co ₃ O ₄ hybrids. C''(ω) vs. logarithm of frequency showing the time response for charging-discharging of graphene variants with (c) CoO and (d) Co ₃ O ₄	55
Figure 27. Charge-discharge profiles of representative CoNP/MLG hybrid for 0.25 A g ⁻¹ , 0.20 A g ⁻¹ , 0.10 A g ⁻¹ , and 0.05 A g ⁻¹	56
Figure 28. Probe approach curves including experimental (solid) and fitting (dashed) for graphene based hybrids with (a) CoO and (b) Co ₃ O ₄	58
Figure 29. Two- and three-dimensional areal scans of representative (a) Co ₃ O ₄ , (b) CoO (c) ErGO, and their corresponding (d) Co ₃ O ₄ and (e) CoO hybrids.....	60
Figure 30. CV curves containing ORR catalysis assisted by representative samples: (a) CoNP/MLG, (b) CoO/ErGO, and (c) Co ₃ O ₄ /ErGO, with corresponding current response at 0.4 V for (d) CoO and (e) Co ₃ O ₄ based hybrids.....	61
Figure 31. (a) cyclic voltammogram for Co ₃ O ₄ /MLG in various glucose concentrations, current response ($i-t$ plots) for chosen hybrids of (b) glucose alone and (c) glucose upon addition of uric acid and ascorbic acid.....	63
Figure 32. Depiction of the structure of glucose and its oxidized form gluconolactone.....	64

LIST OF TABLES

Table 1. Summary of the solutions with their respective concentrations and amounts used for electrochemical deposition of CoNP, CoO, and Co ₃ O ₄	20
Table 2. Circuit elements, solution's resistance- R_s , charge-transfer resistance- R_{ct} , double-layer capacitance- C_{dl} , and Warburg impedance- Z_w , from ac impedance simulation and fitting.....	50
Table 3. Summary of maximum and minimum C_s values obtained from galvanostatic measurements.....	52
Table 4. Summary of fitting parameters the one electron heterogeneous rate constant- K_1 , the multi-electron rate constant- K_2 , and fitting parameters describing more complex convoluted processes relate to charge transfer and mass transport- K_3 and K_4 from probe approach of various cobalt oxide constituents and cobalt oxide/graphene hybrids.....	55

SYNTHESIS, CHARACTERIZATION, AND PROPERTIES OF GRAPHENE-BASED
HYBRIDS WITH COBALT OXIDES FOR ELECTROCHEMICAL ENERGY
STORAGE AND ELECTROCATALYTIC GLUCOSE SENSING

Sara C. Botero Carrizosa

May 2017

79 Pages

Directed by: Sanju Gupta, Matthew Nee, and Darwin Dahl

Department of Chemistry

Western Kentucky University

A library of graphene-based hybrid materials was synthesized as novel hybrid electrochemical electrodes for electrochemical energy conversion and storage devices and electrocatalytical sensing namely enzymeless glucose sensing. The materials used were supercapacitive graphene-family nanomaterials (multilayer graphene-MLG; graphene oxide-GO, chemically reduced GO-rGO and electrochemical reduced GO-ErGO) and pseudocapacitive nanostructured transition metal oxides including cobalt oxide polymorphs (CoO and Co₃O₄) and cobalt nanoparticles (CoNP). These were combined through physisorption, electrodeposition, and hydrothermal syntheses approaches. This project was carried out to enhance electrochemical performance and to develop electrocatalytic platforms by tailoring structural properties and desired interfaces. Particularly, electrodeposition and hydrothermal synthesis facilitate chemically-bridged (covalently- and electrostatically- anchored) interfaces and molecular anchoring of the constituents with tunable properties, allowing faster ion transport and increased accessible surface area for ion adsorption. The surface morphology, structure, crystallinity, and lattice vibrations of the hybrid materials were assessed using electron microscopy (scanning and transmission) combined with energy

dispersive spectroscopy and selected-area electron diffraction, X-ray diffraction, and micro-Raman Spectroscopy. The electrochemical properties of these electrodes were evaluated in terms of supercapacitor cathodes and enzymeless glucose sensing platforms in various operating modes. They include cyclic voltammetry (CV), *ac* electrochemical impedance spectroscopy, charging-discharging, and scanning electrochemical microscopy (SECM).

These hybrid samples showed heterogeneous transport behavior determining diffusion coefficient ($4 \times 10^{-8} - 6 \times 10^{-6} \text{ m}^2/\text{s}$) following an increasing order of CoO/MLG < Co₃O₄/MLG < Co₃O₄/rGO_{HT} < CoO/ErGO < CoNP/MLG and delivering the maximum specific capacitance 450 F/g for CoO/ErGO and Co₃O₄/ rGO_{HT}. In agreement with CV properties, these electrodes showed the highest values of low-frequency capacitance and lowest charge-discharge response (0.38 s – 4 s), which were determined from impedance spectroscopy. Additionally, through circuit simulation of experimental impedance data, RC circuit elements were derived. SECM served to investigate electrode/electrolyte interfaces occurring at the solid/liquid interface operating in feedback probe approach and imaging modes while monitoring and mapping the redox probe (re)activity behavior. As expected, the hybrids showed an improved electroactivity as compared to the cobalt oxides by themselves, highlighting the importance of the graphene support. These improvements are facilitated through molecular/chemical bridges obtained by electrodeposition as compared with the physical deposition.

Chapter 1: Introduction

This chapter provides the organization of the thesis, relevant background, motivation, material description and characterization techniques to lay the foundation for the studies of graphene-based (Gr) hybrids with cobalt oxides (Co_xO_y). The necessity for alternate sources of energy is addressed first to introduce carbon, its allotropes, and hybrids as potential candidate material systems for electrochemical energy conversion and storage. Furthermore, the chapter describes the principles of electrochemical energy storage and conversion relevant to this thesis research and the characterization techniques employed to gain insights concerning the behavior of $\text{Co}_x\text{O}_y/\text{Gr}$ hybrids.

1.1 Organization of Thesis

Chapter 1 provides the necessary background and motivation behind this entire research project and lays down the foundation for the experiments performed in the following chapters. Chapter 2 describes various synthetic (physisorption, electrodeposition, and hydrothermal) approaches, structural and physical property characterization of hybrid electrodes prepared from novel nanomaterials on commercial substrates. The electrochemical properties and scanning electrochemical microscopy-SECM of these hybrids as novel electrochemical electrodes for energy storage and conversion are thoroughly discussed in Chapter 3. These studies were performed to determine their charge storage capacity (specific capacitance), retention rate (charging-discharging), double-layer capacitance (*ac* impedance), interfacial parameters (charge transfer resistance), physicochemical processes at electrode/electrolyte interfaces and imaging (SECM). Chapter 3 also includes an exploration for these hybrids as economically viable advanced electrocatalytic platforms for oxygen reduction reaction

and for enzymeless glucose sensing. Finally, Chapter 4 states the summary and the future prospects of this work. An additional appendix (Appendix A) introduces in-situ Raman spectro-electrochemistry investigations to study charge transfer dynamics where micro-Raman spectroscopy was integrated with electrochemistry as ‘device under test’ approach with corresponding preliminary results. Finally, the conclusions are summarized with subsequent implications of our findings as future prospects

1.2 Motivation and Background

The energy sector has major segments including of nuclear sources, fossil fuels (petroleum, coal, and natural gas), and renewable sources (wind, solar, and geothermal energy).¹ Even though wind and solar energy have shown the potential to generate clean and renewable energy, their intermittent nature poses a problem for consumption on demand. Because the current global need for energy sources is pressing, intense research activity on energy storage and conversion devices has become essential to meet this demand.² Within these, electrochemical systems represent some of the most efficient and environmentally benign technologies.³ Therefore, the work presented here seeks to investigate potential energy-storage materials for alternative clean energy sources. The objective of this work is to design and synthesize a range of graphene-based ‘hybrid’ nanomaterials with tailored interfaces/interphases as high-performance electrochemical electrodes and investigate their structural, physical, and electrochemical properties. These materials, based on graphene and its derivatives in junction with transition metal oxides, are environmentally friendly and display supercapacitive performance including gravimetric and area capacitance, charging/discharging cyclability, and retention over hundreds to thousands of cycles. Furthermore, the experimental approaches employed in

this work are scalable such that they have the potential for usage in real-world applications. Therefore, this work sets a platform of evaluation of carbon-supported hybrids with cobalt oxides for the application of energy conversion and storage.

1.3 Nanomaterials for Electrochemical Energy Conversion and Storage

Nanomaterials are materials on the order of 1 to 100 nm that have shown several advantages over bulk materials.⁴ The structural modifications that equip nanomaterials to outperform bulk materials in energy conversion and storage include higher specific surface area, enlarged band gap, enhanced mechanical strength, and improved charge transport dynamics.^{5,6} These properties are highly desirable for electrodes that have the capability to store and deliver energy efficiently.⁷ Some of the nanomaterials that have been successful in energy devices include metal nanoparticles and carbon-based materials.

1.3.1 Carbon-Based Materials and Graphene

Carbon exists in a variety of allotropes including diamond (sp^3 bonded carbon), graphite (sp^2 bonded carbon), amorphous carbon, fullerenes, carbon nanotubes, and graphene. These forms of carbon can exist in one-, two- and three-dimensions, which allows them to have a wide-range of physical and chemical properties and to be suitable for diverse applications. Even though the most basic arrangements of carbon are diamond and graphite, their structure and, thus, their properties differ completely. While diamond is classified as the hardest material on earth and is an insulator, graphite is known as a soft material and is also classified as a semi-metal. In addition to graphite and diamond (Figs. 1a and 1b, respectively),² other observed forms of carbon include amorphous carbon (a-C) (Fig. 1c),⁸ hydrogenated amorphous DLC (*a-C:H*), tetrahedral

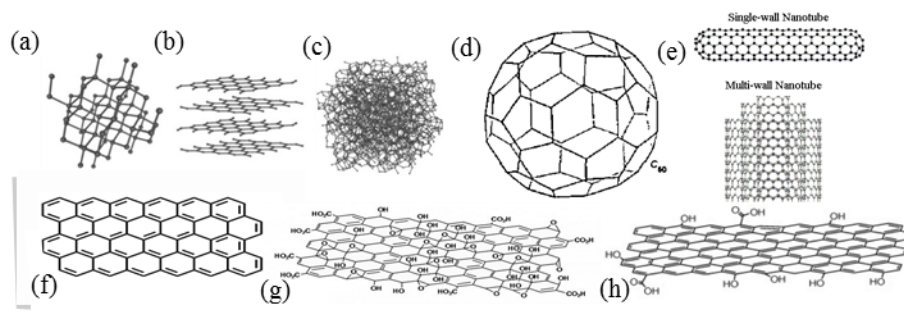


Figure 1. Depiction of the chemical structure of: (a) diamond, (b) graphite, (c) amorphous carbon, (d) fullerene (C_{60}), and (e) SWCNT and MWCNT, (f) graphene; Gr, (g) graphene oxide; GO, and (h) reduced GO; rGO.

amorphous carbon (ta-C), and hydrogenated tetrahedral amorphous carbon (ta-C:H).⁸

Carbon atoms can also arrange into cage-like structures of higher complexity,⁹ classified under the category of fullerenes. This configuration includes the C_{60}

buckminsterfullerene, or “buckyballs,” C_{70} , C_{84} and several other intricate structures,¹⁰

which have been investigated as superconductors, medical treatment and diagnostics, and military armor (Fig. 1d).¹¹ A type of fullerene structure is known as carbon

nanotube, which comprise closed-ended graphene cylinders. A single graphene sheet coiled in a single tube or single wall nanotubes (SWCNT) forms the simplest nanotube structure. Multi-walled nanotubes (MWCNT) can also be obtained upon layering of

concentric sheets onto the SWCNT. SWCNTs and MWCNTs are depicted graphically in

Fig. 1e. Because their radial dimension is on the order of nanometers, nanotubes are

classified as one-dimensional with a longitudinal length in the order of microns. Due to

their structural arrangement, nanotubes exhibit metallic and semiconducting properties, making them suitable for potential applications like field-effect transistors (FETs),

display panels, energy cells, and sensor technologies. Since its discovery in 2004,¹²

graphene has been widely researched because of its unique and comprehensive range of

physical and chemical properties¹³ allowing graphene to be suitable in a variety of applications. Some of the functionalities observed in graphene that qualifies it as an outstanding candidate for energy storage devices (supercapacitors) and electrochemical sensors are slight overlapping of its conduction and valence bands,¹⁴ high mobility of charge carriers ($\sim 20,000 \text{ cm}^2 \text{ V}^{-1} \text{ s}^{-1}$),¹⁵ a high theoretical specific surface area ($2630 \text{ m}^2 \text{ g}^{-1}$),¹⁶ and remarkable mechanical strength (Young's modulus $\sim 1 \text{ TPa}$).¹⁷

Graphene is a 2-dimensional, atom-thick carbon layer obtained from graphite that has a honeycomb-crystal lattice due to the sp^2 hybridized bonding between the carbon atoms (Fig. 1f) and can exist as a single layer (monolayer graphene),¹⁶ bilayer graphene (BLG), trilayer graphene (TLG), few-layer graphene (FLG),¹⁸ and multilayered graphene (MLG).¹⁹ The application of graphene can be extended by modifying its electrical properties through the alteration of its structure. Such modifications can be accomplished by doping and/or introducing surface and edge functional groups, forming graphene derivatives with tailored physical and chemical properties.²⁰ Among the many graphene derivatives, graphene oxide (GO),²¹ chemically reduced GO (rGO),²² and electrochemically reduced GO (ErGO)²³ suitable for opto-electronics,²⁴ bio-sensors,²⁵ fuel cells,²⁶ solar cells,²⁷ and energy storage devices.²⁸

Due to the rupture of the conjugated system (sp^3 hybridization) upon oxidation, which functionalizes carboxyl-COOH, hydroxyl-OH, and epoxide-COC groups along both edge and surface sites, the structure of GO becomes insulating. The facile (chemical, electrochemical, or hydrothermal)²⁹ reduction of GO partially restores the conjugated system (sp^2 hybridization), providing the structure with the ability to conduct

charge again (Figs. 1g and 1h). However, no method can fully reduce GO to pristine graphene, leaving some of the functional edge groups that can affect reactivity and electrical properties.³⁰ For instance, the oxygen on the C=O double-bond from a carbonyl group inductively withdraws electrons from the carbon, making carbon an electrophile; while the oxygen on the C-O bond from a hydroxyl group inductively donates electrons, generating a nucleophilic site. In addition, the appearance of carboxyl and carbonyl groups in GO allows hydrogen bonding, increasing its affinity for water, while the reduction of GO reduces the sites for hydrogen bonding, decreasing its affinity for water. Furthermore, the electrochemical properties of GO and rGO can be altered by controlling the extent of oxidation and reduction of the graphene structure,³¹ enabling interactions and structure-dependent electrochemical and electrocatalytic activity.³² Another functional modification of the structure of graphene is layering graphene onto 3-dimensional networks to increase the electrode's surface area and facilitate charge transfer and ion diffusion as is the case for multilayered graphene on nickel foam (NiFoamMLG).³³

1.3.2 Other Potential Materials

Since the highest performance electrocatalysts (e.g. Pt, Rh) are costly, nonrenewable, and environmentally hazardous, materials like redox-active transition metal oxides that are inexpensive and have relatively low toxicity have shown promise for energy-related applications.^{34,35} Among the many types of electroactive transition metal oxides (e.g. RuO₂, TiO₂, SnO₂, Mn₃O₄/MnO₂, NiO, V₂O₅, Fe₃O₄/Fe₂O₃, MoO₂ etc.),^{36,37} cobalt oxides (CoO and Co₃O₄) can be used as a replacement to current electrocatalysts owing to their accessible synthesis and processing, high specific

capacitance, high conductivity, electrochemical stability, and availability of oxidation states (Co^{3+} , Co^{2+}).^{38,39} Cobalt nanoparticles (CoNP) or cobalt nanocrystals are also attractive due to their electrochemical and electrocatalytic activity in addition to their electronic and magnetic properties.^{40,41} Cobalt nanoparticles exist in crystalline structures including cubic-closed packed (ccp) and hexagonal closed packed (hcp), however, the face-centered cubic (fcc) phase is also reported.⁴² Cobalt monoxide, CoO, consists of Co^{2+} octahedral coordination where the oxygen sublattice is a fcc with ~5% higher oxygen ionic bond packing for rock-salt than for the spinel structure.⁴³ Cobaltous oxide or cobaltic-cobaltous oxide (Co_3O_4) consists of both Co^{2+} and Co^{3+} species occupying tetrahedral and octahedral coordination sites, conforming to a normal cubic spinel structure (Fig. 2).⁴⁴ These structural configurations allow for cobalt oxide polymorphs to be potential candidates for electrocatalytic applications.⁴⁵

1.3.3 Hybrid Nanomaterials

The inefficiency of alternate energy sources compared to conventional, non-renewable energy sources serves as an incentive for developing novel multifunctional materials for advanced electrochemical electrodes and technologies for energy conversion and storage.⁴⁶ Since the performance of carbon-based (*e.g.* GO, rGO, ErGO, MLG) supercapacitors is limited due to self-aggregation and local topological defects,

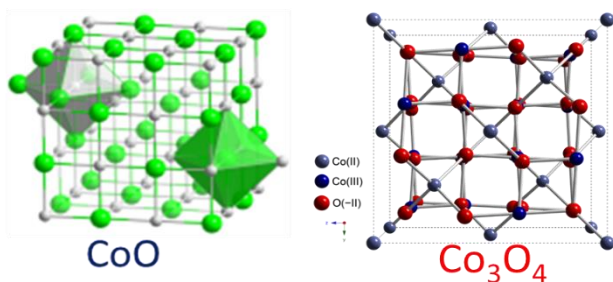


Figure 2. The crystal structure for both CoO (fcc) and Co_3O_4 (cubic spinel).

their integration with pseudocapacitive transition metal oxides offers alternatives for enhanced supercapacitive performance. This results in formation of hybrid materials with tailored properties (surface morphology, composition, structure, etc.) and interfaces.³¹ Various studies have provided relevant insights on the improvement in electrochemical performance (*e.g.* specific capacitance, charge-discharge cycling, and charge transport) of such hybrid materials systems.^{29,47} Although the exact interaction between the nanostructure transition metal oxides and carbon-based supports have yet to be determined, the possible interactions (noncovalent, defect related, and covalent) are illustrated in Fig. 3. While Fig. 3a shows direct contact of the transition metal oxide (CoO or Co_3O_4), suggesting weak or absent non-covalent interactions between the surfaces, Fig. 3c illustrates the possible coordination of the respective defect sites for metal oxides and the carbon-based support, creating a non-covalent interaction. Bonding

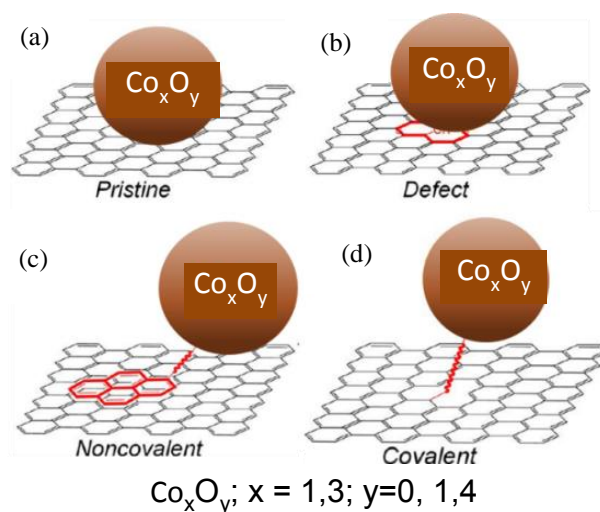


Figure 3. Schematic illustration of transition metal oxides–carbon-based support interfaces: (a) pristine interface or direct contact; (b) bonding between atoms of transition metal oxide and the defect sites of carbon-based support; (c) noncovalent interactions of functional moieties of carbon-based support with transition metal oxides, and (d) covalent bonding of carbon-based support and transition metal oxide.

is another likely possibility in which either multiple dangling atoms of the transition metal oxide may bind to the defect sites of the carbon-based support (Fig. 3c) or the interaction is established by a single covalent bond between the two materials. The work in the thesis aims to design and develop novel hybrids based on graphene-based and cobalt oxides keeping in view of optimizing their electrochemical and electrocatalytic properties.

1.4 Electrochemical Principles

Electrochemistry, the study of electrical energy in relation to chemical reactions, is a powerful tool to create and investigate novel materials for energy conversion and storage. The key to understand an electrochemical process is the electron/ion or charge transport occurring at the interfacial boundary between electrode and electrolyte. Experimentally, the electrode-electrolyte interface resembles the behavior of a capacitor. However, at the interface, charge is stored in the electrical double layer (figure 4). This double layer comprises multiple layers: the inner Helmholtz layer, inner layer where specifically absorbed species -ions or molecules- reside, the outer Helmholtz layer, the

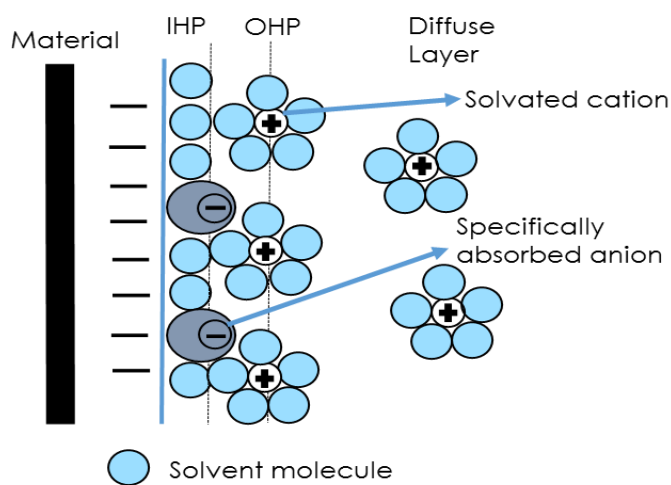


Figure 4. Depiction of the different layers (inner Helmholtz layer- IHP, outer Helmholtz layer-OHP, and diffuser layer) on a EDLC.

following layer where solvated ions or nonspecifically absorbed ions are present, and diffuse layer, layer which extends to the bulk of the electrolyte solution and includes some of the nonspecifically absorbed ions. Such capacitive behavior can be exploited for energy storage (supercapacitors, pseudocapacitors) and conversion (rechargeable secondary batteries) and electrocatalysis. Moreover, the double layer structure can affect the absorption of particular ionic species in solution (sensing).

To assess the electrochemical properties of the electrodes, a three-electrode electrochemical cell and a coin cell configurations are commonly used. In general, they consist of a working electrode of which the electrochemical properties are measured with respect to a reference electrode (constant composition and fixed potential), and a counter electrode (aids in partially removing the voltage drop originated from the resistance of the solution and the current placed between working and counter electrodes (iR_s)) in the presence of an electrolyte (low ionic resistance).⁴⁸

1.4.1 Supercapacitors and Pseudocapacitors

Supercapacitors (SCs) are subject to much research because they are battery-complimentary devices due to their longer life cycles and higher power density.⁴⁹ Energy storage in a SC is of two types: electrochemical double-layered capacitors (EDLCs) in which accumulation of charge occurs in the electrode/electrolyte interface, and pseudo-capacitors in which the storing of energy is based upon the redox reactions generated at the surface of the electroactive material.⁵⁰

The energy (E) stored in SCs follows the same equation of direct current capacitors, where E is proportional to half of the product between cell capacitance (C) and the square of applied voltage (V):

$$E = \frac{1}{2} * C * V^2 \quad (1)$$

Cell capacitance for SCs with identical electrodes can be obtained as a constant from the ratio of the change in charge and the change in voltage, where charge can also be defined with respect to current and change in time:

$$C_{cell} = \frac{\Delta q}{\Delta V} = \frac{i * \Delta t}{\Delta V} \quad (2)$$

To compare various SC devices, C_{cell} can be expressed in units per mass (specific cell capacitance, C_{spec}) which modifies Eq. 2 by dividing the total mass of both electrodes.⁴⁹

1.4.2 Rechargeable Secondary Batteries

A battery is a collection of electrochemical cells arranged to offer a particular voltage (series) and capacity (parallel) to ultimately provide electrical energy from the chemical reaction occurring at the electrodes. One of the most common types is Li-ion battery in which lithium ion is the charge carrier between the two electrodes due to its high mobility and energy density. Each electrochemical cell is composed of two intercalating Li-ion electrodes (negative and positive) separated by an electrolyte that conducts Li^+ and a separator where the electrodes are linked externally by a power source.⁵¹ These batteries are widely marketed for their portability and high energy density as a primary power source while SCs serve as an alternate power source. However, the properties of Li-ion and SC electrodes can be coupled for multifunctional energy storage devices.⁵²

1.4.3 Electrocatalysis and Sensing

Electrocatalysis is a process in which an electrode surface has the capability of improving or accelerating the kinetics of an electrochemical reaction. Oxygen reduction

and hydrogen evolution are two major electrochemical processes that can be catalyzed for renewable energy conversion in fuel cells.⁵³ In particular, alkaline fuel cells create a constant current flow by reducing incoming oxygen (O_2) with the reduction current flowing through the electrode. The resulting reduced ionic species (OH^-) will travel to the cathode, due to the potential gradient, and consequently oxidize incoming hydrogen (H_2), creating an oxidation current (Fig. 5).⁵⁴ In addition, the electrochemical properties of an electrode, including conductivity, size, and high surface area can enable electron transfer dynamics with particular species or analytes in solution, allowing faster and sensitive detection in their presence or upon addition due to the change in electrode current and/or potential.⁵⁵ For example, an electrochemically active material can sense the presence of glucose by oxidizing/reducing it without requiring an enzyme which may provide a more affordable device that can be disposable.³⁸

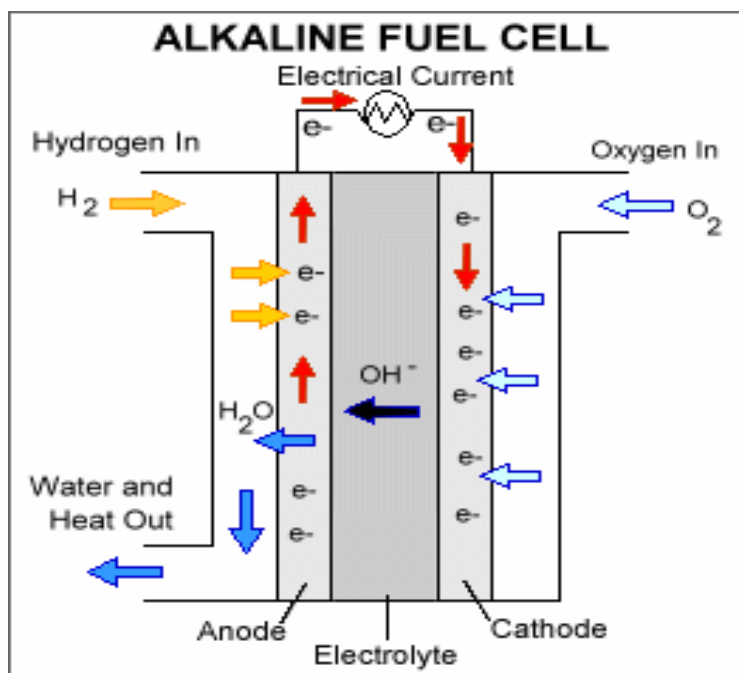


Figure 5. Scheme of an alkaline fuel cell. Adapted from Ref. 54

1.5 Characterization Techniques

A variety of complementary structural and physical property analytical characterization tools were used including scanning electron microscopy (SEM) combined with energy dispersive X-ray spectrometry (EDS), transmission electron microscopy (TEM), Raman spectroscopy (RS), X-ray diffractometry (XRD), and atomic force microscopy (AFM) to probe the quality of the synthesized hybrids prior to investigating their electrochemical properties. The electrochemical properties include cyclic voltammetry (CV) and impedance spectroscopy (EIS), besides scanning electrochemical microscopy (SECM) to gain insights into the electrodes surface kinetics and physical-chemical processes at the electrode/electrolyte interfaces.

1.5.1 Electron Microscopy: Surface Morphology and Microscopic Structure

Scanning Electron Microscopy: SEM (Model JEOL 5400LV; MA, USA) was used to obtain qualitative information of the surface morphology and to identify the topological features at a microscale. SEM was operated at primary electron accelerating voltage (V_{acc}) of 10 kV, in a secondary electron imaging mode (SEI) at constant current of 45 mA. Energy dispersive X-ray spectrometry (EDS) was also performed using the SEM, confirmed the composition of the materials in hybrids.⁵⁶

Transmission electron microscopy and selected area electron diffraction (SAED): The measurement of TEM images provided nanoscale structure and morphology that help determining tomography and interplanar spacing for capturing interfaces.⁵⁷ TEM images and SAED patterns were collected using a JEOL 1400Plus operating in cryo-EM, SAED, tomography and energy dispersive x-ray modes at 100 kV and 1 nA with a JEOLBe specimen holder, a IXRF Systems control software and

hardware, and a Gresham SiLi detector with Moxtek AP3.3 window. SAED used a 0.23- μm aperture, with small spot size and spread beam which increases the electron coherence length of the samples allows the beam to transmit through the sample generating a diffraction pattern. Electron tomography used single axis tilt-series which were collected and processed using “SerialEM” IMOD and eTomo software (developed by the University of Colorado-Boulder, USA). An 8M pixel Advanced Microscopy Techniques bottom-mounted digital camera completed the tomography software. TEM samples were prepared by depositing particulates dispersed in ethanol on commercial carbon Cu grids (Ted Pella, CA, USA) and allowed to air-dry.

1.5.2 X-Ray Diffraction and Raman Spectroscopy: Crystal and Lattice Structure

X-ray diffraction: The XRD provided insight into the crystallinity of cobalt oxides and graphene derivatives while measuring the average crystal structure (bulk).⁵⁸ The XRD patterns were obtained using a Siemens Model D2000 instrument (now Thermo Scientific, MA, USA). The x-ray diffractograms were acquired in Bragg-Brentano geometry ranging 2θ from 10° to 70° using Cu K_α ($\lambda = 1.5405 \text{ \AA}$) x-ray source operating at current of 40 mA and voltage of 45 kV. Samples were run at scan rate of $0.02^\circ/\text{s}$ with exposure time of 2 s.

Raman Spectroscopy: Raman spectra were measured to determine the lattice vibration and structural features of the hybrid surfaces.⁵⁹ To record the Raman spectra, a micro-Raman spectrometer (Model InVia; Renishaw, UK) equipped with an excitation laser of wavelength 633 nm ($E_L = 1.92 \text{ eV}$) and $\sim 4\text{-}6 \text{ mW}$ incident on the sample, with edge filters cutting at $\sim 100 \text{ cm}^{-1}$ was used. The Raman light from the sample was collected in a backscattering geometry, transmitted by a beam splitter, and detected by a

CCD camera. A 2- μm spot size was obtained using a 50x objective lens. An edge filter removed the laser excitation, filtering the reflected light then sent to a spectrometer.

Raman shift was measured from 110 to 3400 cm^{-1} for Co containing hybrids, while for Co polymorphs, the shift was measured between 100 and 800 cm^{-1} .

1.5.3 Electrochemistry and Electrochemical Microscopy

All the electrochemical tests were measured using an electrochemical workstation (Model 920D CH Instruments, Inc.) in a custom-designed three-electrode electrochemical cell with Ag/AgCl reference electrode and a platinum (Pt) counter electrode.

Cyclic Voltammetry: CV is commonly the first technique to assess the electrochemical kinetics of electrodes and of electroactive species. CV measures the response (current, i) of the working electrode with applied bias (potential, V), forming a cyclic voltammograms (i -V curves) that provide information concerning ion transport and electron transfer kinetics. Moreover, by varying scan rate, one can observe the electrode surface kinetics as ions interact at the interface in direct proportionality to the scan rate, obtaining parameters such as diffusion constant, gravimetric capacitance, etc.⁶⁰

CV was measured for all the samples in 1 M KOH electrolyte with potential ranging from -0.2 V to +1.0 V at a varying scan rate of 10, 20, 50, 100, 200 mV/s. To prevent decomposition of the $\text{Co}_3\text{O}_4/\text{GO}$ hydrothermally synthesized hybrid, CV was measured in 0.1M KOH with potential ranging from -0.1 V to +0.65 V at a varying scan rate 1, 5, 10, 20, 50 mV/s. Within the CV mode, the materials were cycled at a scan rate

of 50 mV/s for first, second, and fifth cycles to observe their electrocatalytic response to oxygen reduction reaction (ORR) from potential 0.0 to 0.8 V.

Electrochemical Impedance Spectroscopy: The EIS mode provides the components of impedance (real, Z' , and complex, Z''), the phase behavior (ϕ) with frequency (ω), giving rise to Nyquist plots (Z'' vs. Z'). Impedance and phase behavior were measured over a frequency range from 0.01 Hz to 98000 Hz and at potentials of 0.1 V, 0.2 V, 0.3 V, and 0.4 V, depending on the sample, with 5mV ac amplitude. To derive various physical parameters of the working electrodes, circuit simulations are carried out to obtain solution resistance (R_s), charge transfer resistance (R_{ct}), double-layer capacitance (C_{dl}), and Warburg impedance (Z_w). Using the low-frequency limit of the Nyquist plot, low-frequency capacitance (C_{lf}) and time response from the imaginary part of capacitance (C'') were also be obtained.⁶¹

Amperometry: This technique records the electrode current at a constant potential, providing current vs. time (i - t) profiles which can be used for electrochemical synthesis (2.2.2) and sensing behavior among others.⁶²

Chronopotentiometry: Chronopotentiometry is a current-controlled technique that monitors the potential response with respect to time of the electrode at a constant current (i). As the species neighboring the electrode are reduced due to the continuous flux of electrons, the potential is changed until the oxidized form of the species is consumed. Five sets of galvanostatic measurements were performed on each sample with initial current of 0.25 A g⁻¹ for 25 cycles, followed by variations in current of 0.20 A g⁻¹, 0.10 A g⁻¹, 0.05 A g⁻¹, 25 cycles each, and 0.25 A g⁻¹ for the last 10 cycles. Chronopotentiometry measurements allow the assessment of the stability while the

electrodes charge and discharge and provide a different method to calculate specific capacitance.⁶³

Scanning Electrochemical Microscopy (SECM): SECM is an advanced electrochemical imaging technique that probes and maps the electrochemical response (change in current) of electrodes locally (alternatively, micro-electrode configuration, Fig. 6a in contrast to traditional electrochemistry (macro-electrode configuration). The reaction occurs at the tip which is controlled by the piezo positioner (a platinum disk sealed in glass and polished) as potential is applied independently for substrate and tip by a bipotentiostat workstation.

For probing, the tip is close to the substrate, avoiding contact while immersed in electrolyte containing an electroactive substance (O) of known concentration (C_O^*) and diffusion coefficient (D_O). When the tip is far from the substrate, the steady-state current ($i_{T,\infty}$) obeys:

$$i_{T,\infty} = 4nFD_O C_O^* a \quad (3),$$

where n is stoichiometric number of electrons consumed in the electrode reaction, F is Faraday's constant, and a is the radius of the tip electrode (Fig. 6b). When the tip is placed closer to the substrate, the current can either decrease (O diffusion to the tip is blocked by the substrate, the concentration of reduced species, R, rises) or increase (O diffusion to the tip is facilitated by the substrate, *e.g.* substrate oxidizes R to O) (Figs. 6c and 6d, respectively).

In SECM, probe approach provides an assessment of the conductivity of the electrode by measuring the current at the tip (i_T) as a function of the distance between

the tip and the substrate (6c and 6d) while in the presence of a redox mediator (Ferrocene methanol, FcMeOH). The behavior of the curves can be modeled after

$$I_T(L)_{ins} = \left[0.292 + \frac{1.5151}{L} + 0.6553 \exp\left(-\frac{2.4035}{L}\right) \right] \quad (4)$$

$$I_T(L)_{cond} = \left[0.68 + \frac{0.78377}{L} + 0.3315 \exp\left(-\frac{1.0672}{L}\right) \right] \quad (5),$$

having the normalized tip current ($I_T = i_T / i_{T,\infty}$) as a function of normalized distance ($L = d/a$).⁴⁸ These curve simulations using Eq. (4) and (5) provide a qualitative standard to compare the conducting character of the substrate (Eq. 4 for insulating substrate and Eq. 5 for conducting substrate). In addition, curve fitting of probe approach provides values of one electron and multiple-electron heterogeneous rate constants.

The parameters of polarity one for probe approach were potential at the tip (V_T) of +0.4 V and potential at the substrate (V_S) of -0.5 V. For polarity two, the same magnitudes were used but with opposite signs *i.e.* $V_T = -0.4$ V, $V_S = +0.5$ V. The microscopy feature of the SECM was also used by applying the same polarities for an area of $400 \times 400 \mu\text{m}^2$ to map the electrochemical behavior of the samples using FcMeOH as a potential redox mediator. Since SECM relies on the uniformity of the

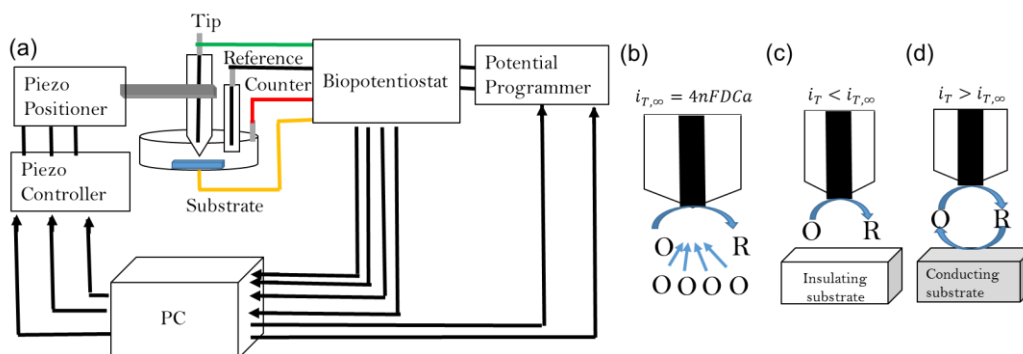


Figure 6. (a) Scheme of the micro-electrode arrangement for SECM and illustration of SECM principles when (b) tip is far from the substrate, (c) and (d) tip is near the substrate adopted from Ref. 48

substrate and without holes, samples deposited on Ni foam were not measured as they were challenging.

Chapter 2: Synthesis and Structural Characterization of Graphene-based Hybrids

In this chapter, the synthesis of graphene-based hybrids with cobalt oxide polymorphs (CoO and Co₃O₄) and cobalt nanoparticles (CoNP) is described. Physical deposition, electrochemical deposition, and hydrothermal synthesis were used to produce the corresponding hybrids which were characterized with various complimentary analytical techniques, including electron microscopy, x-ray diffraction, and micro-Raman spectroscopy.

2.2 Experimental Synthetic Approaches

2.2.1 Physical Deposition

Graphene-based supports (GO and rGO) were decorated with cobalt oxide polymorphs (CoO and Co₃O₄) through physisorption. As previously discussed, the fundamental understanding of the interfacial interactions between the TMeONP and the graphene-based supports is yet to be established. The interaction through physical deposition was primarily attributed to direct contact and non-covalent interactions between the functional groups of the graphene derivative and the cobalt oxide polymorph. For synthesis of GO, rGO and their hybrids with nanoscale powder of cobalt oxide polymorphs, 10-mL dispersions of 0.085 mg/mL of GO (and rGO) and 0.1 mg/mL of CoO and Co₃O₄ were prepared in DI (Milli-Q) water. GO's preparation followed the modified Hummer's method. Thus, rGO was obtained by chemical reduction of GO using hydrazine monohydrate.^{64,65,66} Each solution was stirred for approximately 1 h at room temperature, followed by ultrasonication for around 40 min. The dispersions of graphene-based materials were mixed separately with each cobalt oxide dispersion in 3:1 ratio by volume, creating hybrid solutions employed in this study to determine an

optimized configuration through ultrasonication for 30 min. The samples were obtained by drop-casting each of these mixed dispersions into thin layers on commercial silicon (Si (001)) substrates coated with 285 nm of SiO₂ of approximately 1 cm², allowing the samples to air dry. This method leads to strong physisorption, improving the electrochemical and electrocatalytic activity/reactivity. The samples prepared were as follows: GO (S1), rGO (S2), CoO (S3), Co₃O₄ (S4), S1+S3, S1+S4, S2+S3, and S2+S4.

2.2.2 Electrochemical Deposition

Electrochemical deposition affords chemical adsorption by increasing the interaction (and potential binding) of the graphene-based support and the cobalt oxide polymorph enhancing the electrochemical/ electrocatalytic properties of the electrode while keeping a high surface area. To synthesize thin films of rGO and GO for further electrochemical reduction of GO (ErGO) and electrochemical deposition of the polymorphs of cobalt, 10-mL dispersions of 0.7 mg/mL of GO and 30 mg/mL of rGO were prepared in DI (Milli-Q) water. The preparation of GO followed Hummer's method,⁶⁷ and its chemical reduction with hydrazine monohydride yielded rGO. Both dispersions were stirred for around 1 h at room temperature and ultrasonicated for 15 min. The thin films of each graphene-based material were made by drop-casting and were air-dried on indium tin oxide (ITO) coated glass substrates. ErGO was obtained by reducing a GO sample through amperometric technique at -0.9 V potential⁶⁸ in a conventional three-electrode cell with a platinum counter electrode and a silver chloride reference electrode (Ag/AgCl) immersed in a 1 M NaCl buffer solution of 11.85 pH for 20 minutes.

CoO, Co₃O₄, and CoNP were deposited on the surface of each graphene-based material (GO, rGO, ErGO, and nickel foams industrially coated with multilayer graphene (NiFoamMLG)) using the amperometric technique. For electrodeposition of cobalt oxide polymorphs and CoNP the reference was Ag/AgCl, the counter electrode was glassy carbon rod for Co₃O₄ and CoNP and standard steel (SS321) for CoO, the potential was -1.4 V for CoNP, -1 V for CoO, and +1 V Co₃O₄, and the time was 5400 s for CoNP and 400 s for CoO and Co₃O₄, respectively Figs. 7 and 8).

The solutions used in the depositions are given in Table 1. In addition, each

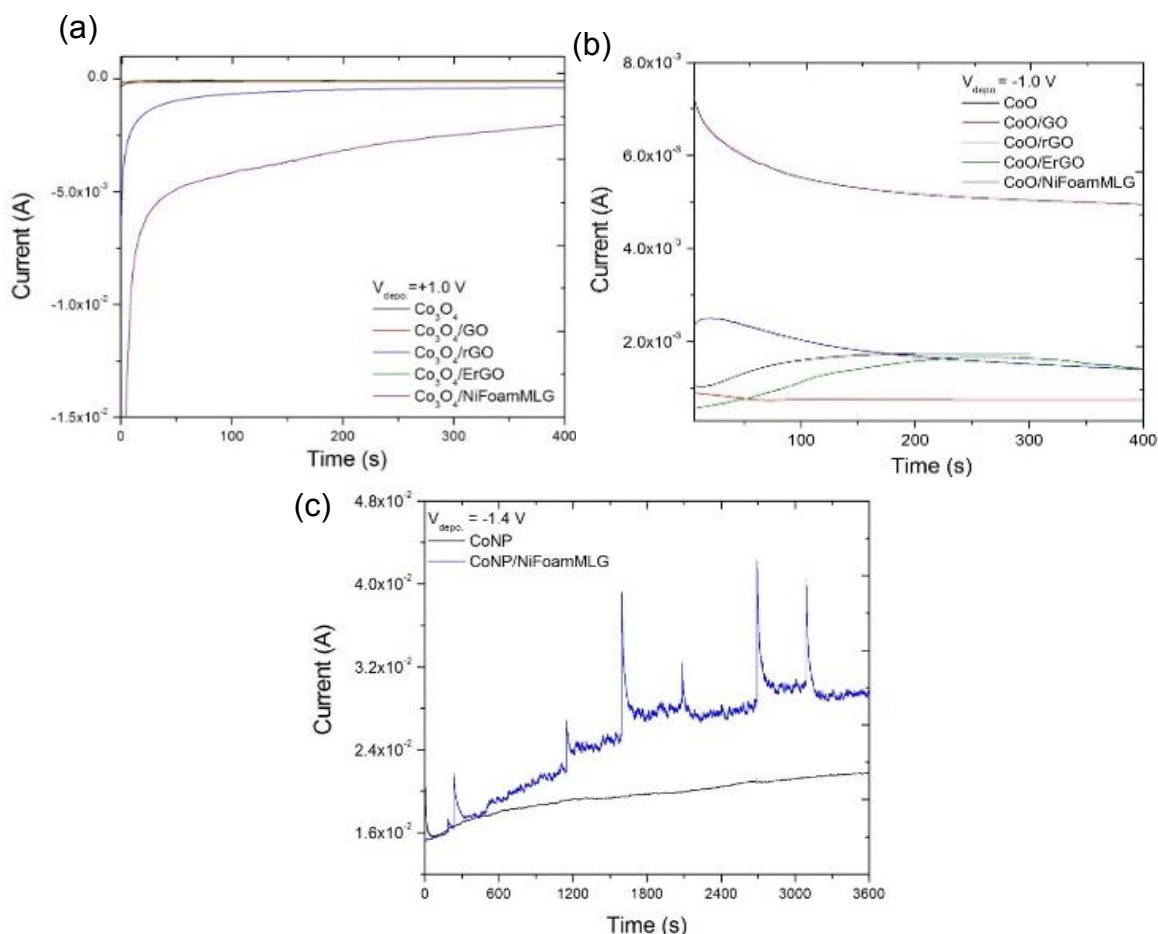


Figure 7. Amperometric plots (*i*-*t* curves) for electrochemical deposition of Co oxide polymorphs (a) Co₃O₄ and (b) CoO and (d) Co nanoparticles alone and on various graphene-supports.

cobalt polymorph was deposited alone on ITO glass, SS321, following the same approach.

Table 1. Summary of the solutions with their respective concentrations and amounts used for electrochemical deposition of CoNP, CoO, and Co₃O₄

Polymorph	Electrolyte
CoNP	100-mL of 0.05 M and pH 7 phytic acid + 100-mL of 0.8 Mm cobalt nitrate hexa- hydrate (Co(NO ₃) ₂ 6H ₂ O) in DI water.
CoO	100 mL of 0.05 M Co(NO ₃) ₂ .6H ₂ O in DI water.
Co ₃ O ₄	30 mL of 0.05 M Co(NO ₃) ₂ .6H ₂ O in DI water + 30 mL of 0.05 M sodium acetate tri-hydrate (NaC ₂ H ₃ O ₂ 3H ₂ O).

To ensure the crystallization of the polymorphs, the samples (except the ones on Ni foam) were subject to heat treatment at 200 °C for 20 min under vacuum. After annealing, the samples cooled in the vacuum furnace for 10 min. Then, the samples were removed from the furnace and cooled to room temperature. **Figure 8.** Schematic

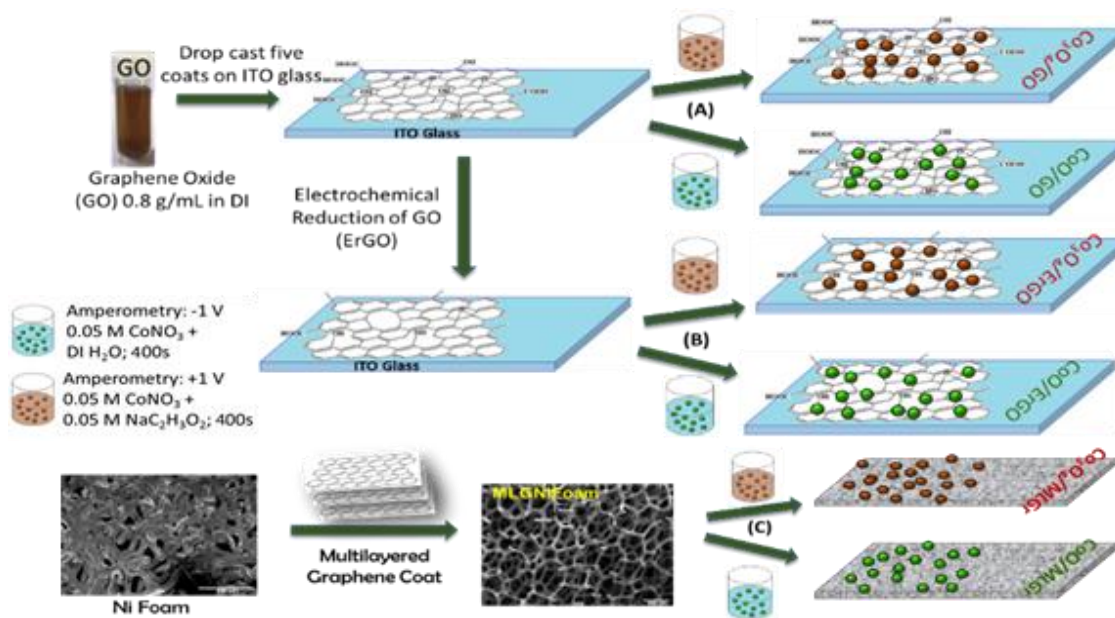


Figure 8. Schematic illustration of electrochemical deposition through amperometry mode of cobalt oxide polymorphs on GO, ErGO and MLG with corresponding parameters.⁶⁸

illustration of electrochemical deposition through amperometry mode of cobalt oxide polymorphs on GO, ErGO and MLG with corresponding parameters.⁶⁸

2.2.3 Hydrothermal Synthesis

Through hydrothermal synthesis, a three-dimensional network is created where the cobalt oxide polymorphs can be completely embedded in the GO and rGO architectures, increasing the specific surface area, thus enhancing the interfacial interactions and improving the electrochemical coupling of the composite materials. Hybrids of Co_3O_4 with GO and rGO were synthesized using this approach. To obtain the GO composite, a 10-mL dispersion of 40 mg of GO was prepared in 99.5% ethanol. The solution was mixed with 10 mg of $\text{Co}(\text{C}_2\text{H}_3\text{O}_2)_2$, followed by an addition of 6 mL of DI water. Similarly, the rGO composite was obtained by preparing a 20.4-mL dispersion of 68 mg of rGO in 99.5% ethanol that was mixed with 17 mg of $\text{Co}(\text{C}_2\text{H}_3\text{O}_2)_2$, and followed by an addition of 11 mL of DI water. Both mixtures were ultrasonicated for 1 h, then heated and stirred at 80°C for 8 h. Once stirred, each dispersion was transferred to individual autoclaves and hydrothermally treated at 150°C for 3 h and later cooled to room temperature. The resulting powders obtained (Co_3O_4 -GO, 25 mg and Co_3O_4 -rGO 111 mg) were taken as 80% to create a mixture with 10% carbon black and 10% poly vinylidene fluoride (5 mg and 11 mg, respectively). Both mixtures were individually subjected to vigorous stirring with 1-methyl-2-pyrrolidinone for 2 h to obtain the Co_3O_4 /GO and Co_3O_4 /rGO composites. Co_3O_4 /rGO composite was coated on ITO, Ni Foam, copper foil, aluminum foil, and SS321 and Co_3O_4 /GO composite was coated on copper foil and aluminum foil. The samples were air dried for 24 h (Fig. 9).

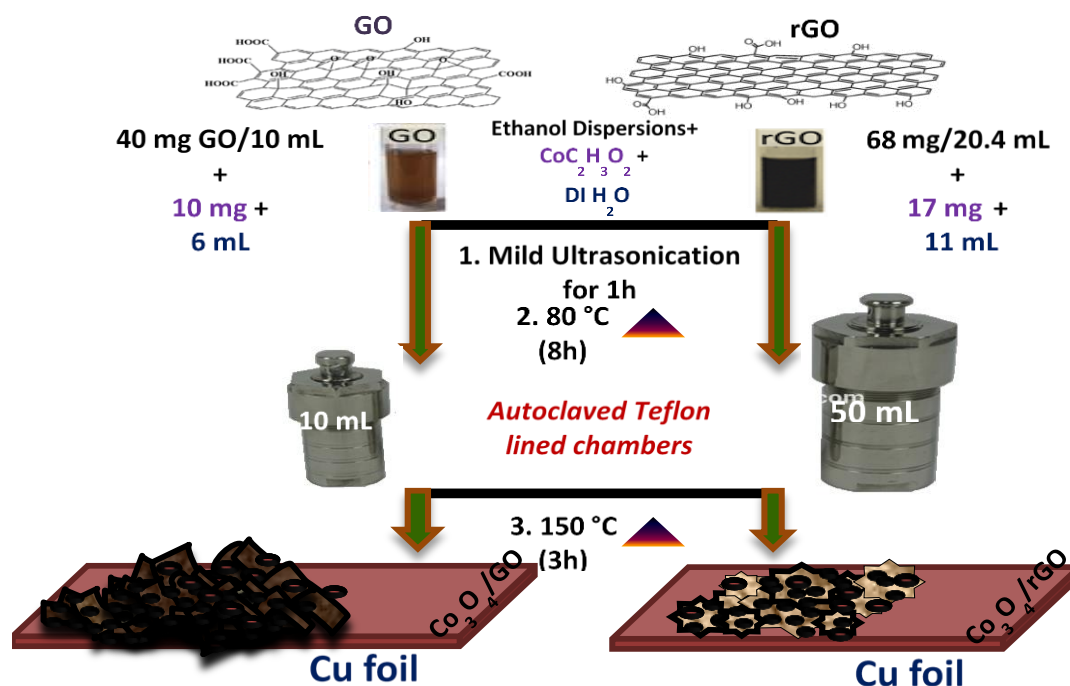


Figure 9. Illustration of hydrothermal synthesis of Co_3O_4 embedded on GO and rGO architectures.

2.3 Results and Discussion

Compared with the overall direct hybrid morphology, the effective characterization of cobalt oxide–graphene interfaces is challenging. The interfacial interactions are key in determining the properties and applications; therefore, the interface study becomes a primary need to stimulate the advancement of graphene-based hybrid material systems.⁶⁹ The following results and discussion correspond to the physically deposited hybrid nanomaterials.

Figure 10 shows SEM micrographs at various length scales of constituents (GO, rGO, CoO and Co_3O_4) and of hybrids (CoO/GO , CoO/rGO , $\text{Co}_3\text{O}_4/\text{GO}$ and $\text{Co}_3\text{O}_4/\text{rGO}$). The images display distinct surface morphology growth, particle size, and type variation (radiated spherulite versus spherical), rGO flakes size distribution and

homogeneity/uniformity of densely packed thin films. Numerous agglomerated nanoparticles with varying shapes are observed, ranging in diameter between 20 and 100 nm. BEI images (not shown) and EDS of CoO/GO and Co₃O₄/GO were measured,

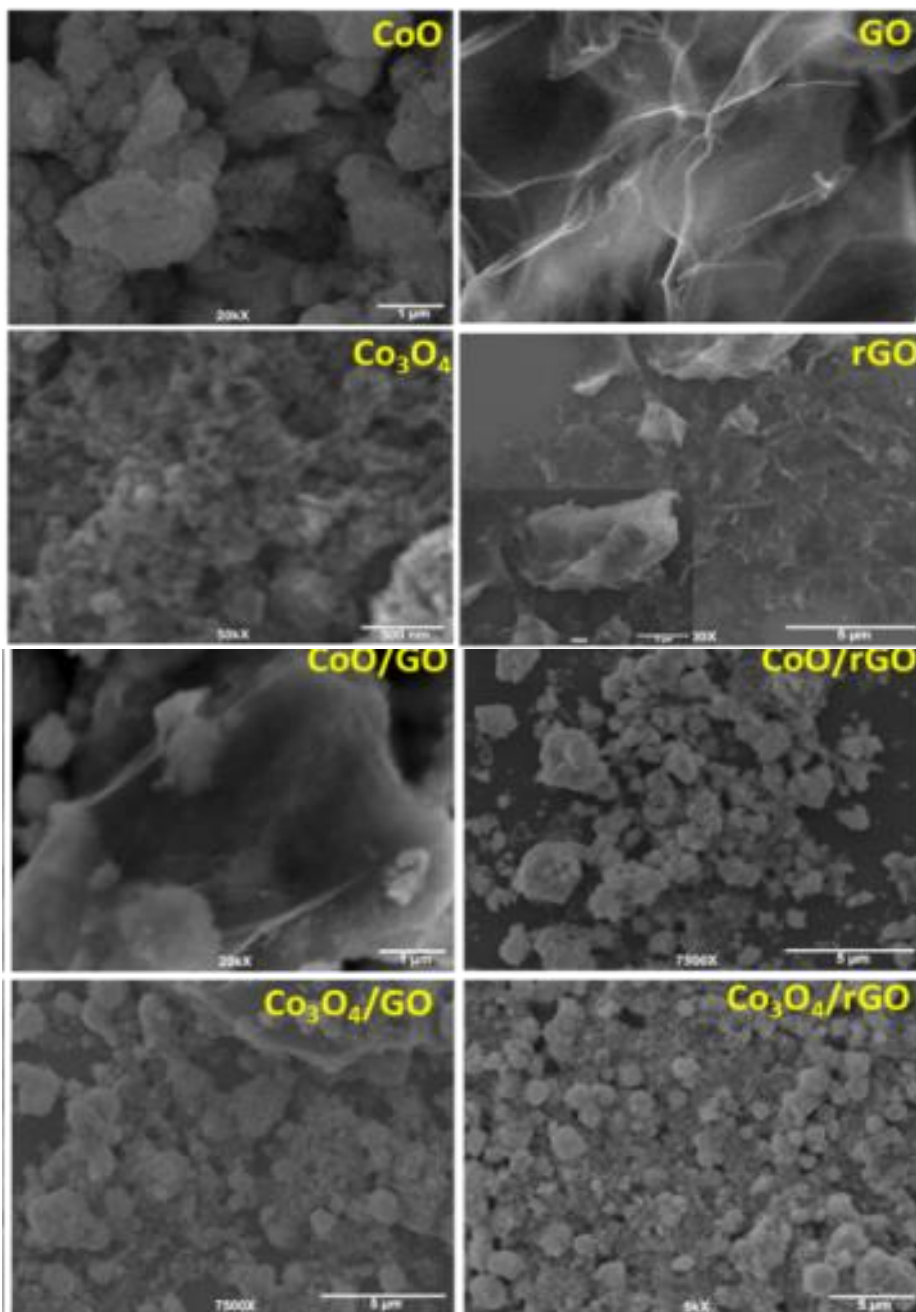


Figure 10. SEM images of GO and rGO and their hybrids with CoO and Co₃O₄. (Scale bars are shown at the bottom of the images).

revealing elemental composition (grey, low Z C and O *versus* dark, high Z Co). The analysis of EDS confirmed the elemental composition of the crystal to be C, Co and O with a molecular formula of Co_3O_4 , including 80% Co_2O_3 and 20% CoO . These results agree with a partially mixed system verified by XRD discussed below. The Co/C ratio was determined to be 0.78 atomic percent (*at.%*) and 0.02 *at.%* in CoO/GO and $\text{Co}_3\text{O}_4/\text{GO}$ hybrids, respectively. This indicates that for every carbon there is 0.0078 Co and 0.004 Co in CoO/GO and $\text{Co}_3\text{O}_4/\text{GO}$ hybrids, respectively.

TEM images were also taken to determine the nanoscale surface morphology at different magnification along with SAED ring / spots and intensity patterns (Fig. 11).

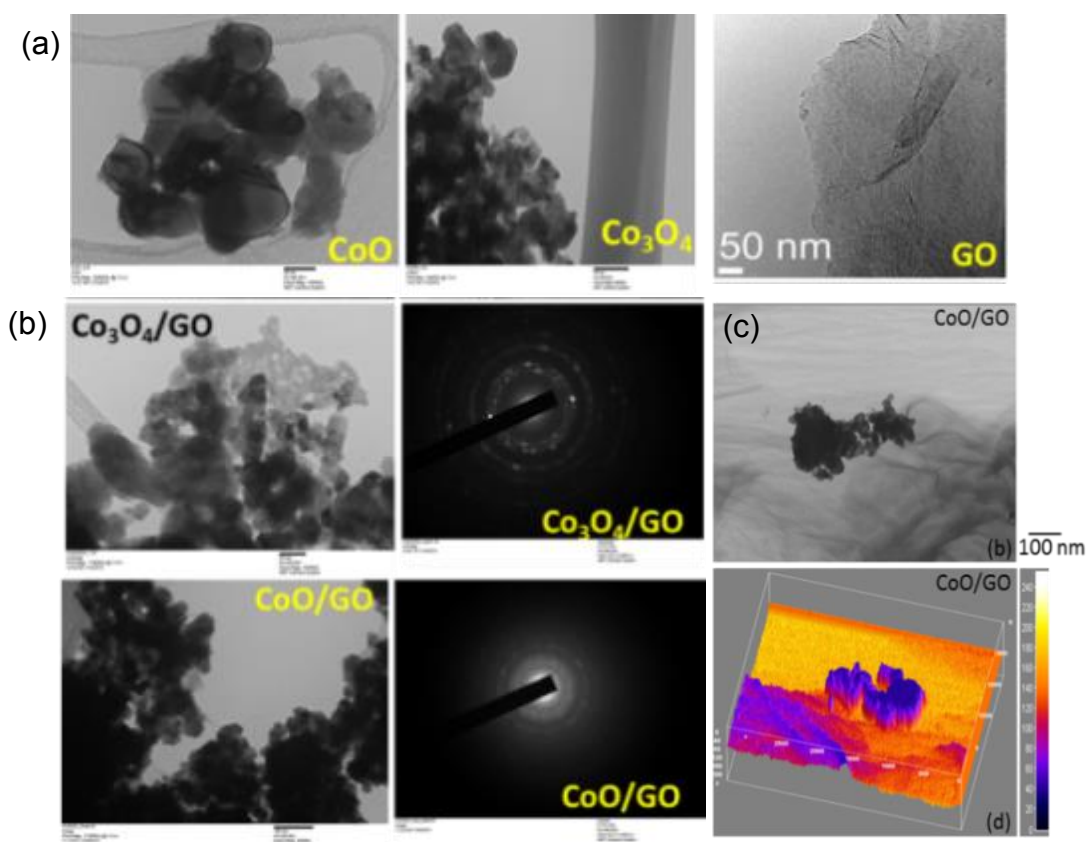


Figure 11. TEM images for (a) CoO , Co_3O_4 , and GO , (b) representative hybrids $\text{Co}_3\text{O}_4/\text{GO}$ and CoO/GO with corresponding SAED patterns, and (c) the electron tomography three-dimensional images for CoO/GO hybrid is included (Scale bars are shown at the bottom of the images).

The intensity pattern of the graphene ring is included as a reference, showing that most of the peaks of hybrids contain graphene and graphene oxide peaks at 1.06 Å, 1.23 Å, 1.71 Å, 2.12 Å and 4.41 Å.⁷⁰ In the TEM images, crystalline defects like stacking faults and dislocations are not seen, and from the surface morphology at nanoscale, the loading of cobalt oxide nanoparticles onto the nanosheets/nanoedge/nanofolds of GO and rGO is apparent. In agreement with the indexed XRD discussed below, the SAED pattern displays quasi-single crystalline nature of Co oxides with rock salt and spinel structure. Fig. 11a shows the overall morphology of CoO_x nanoparticles which consist of intertwined aggregates that on occasion are nanooctahedrons shaped crystallites containing two inverted pyramids attached at their square base and are bounded by eight triangular facets in the case of Co₃O₄ nanoparticles or are either cubed-shaped or spherical in the case of CoO. In addition, the uniform anchoring of the nanoparticles on the graphene sheets/flakes/nanowalls is observed from these images. On one hand, the enlarged TEM image shows lattice fringes with interplanar spacing *d* of 0.392 nm and 0.80 nm, corresponding to the (311) planes of Co₃O₄ crystals and 0.279 nm, which equals the lattice constant of the {400} plane of Co₃O₄. On the other hand, the well-resolved lattice fringes / rings in SAED have an interplanar spacing of 0.45 nm, 0.246 nm, and 0.213 nm in agreement with the distance of (111) (200) and (220) planes for CoO. Overall, the majority of these patterns share a dominant crystal phase with random orientation that appears to have fcc-type rings (space group, *Fm* $\bar{3}$ *m*).^{71,72} An attempt is made to image the graphene-cobalt oxide interface using electron tomography (see Fig. 11b) exhibiting the physical adsorption in three-dimensional TEM image.

XRD is employed to assess the crystallinity and structural phases in different forms as well as determining lattice spacing (d_{hkl}) and crystallite or grain size (L_{hkl}). On one hand, the XRD pattern of GO is mainly represented by a single broad peak at $2\theta = 16.6^\circ$ (002), corresponding to an interlayer distance of 0.74 nm (Fig. 12a). Thus, GO shows larger interplanar spacing than that of graphene, which can be the consequence of the lattice expansion consistent with oxidation of the graphene sheets, intercalation of water molecules and other functional moieties held in the interlayer galleries of hydrophilic GO. On the other hand, the pattern of rGO includes a broad reflection at 24.5° (002) which corresponds to interplanar spacing of 0.36 nm that can be attributed to disorderedly stacked or restacked graphene nanosheets and a peak at $\sim 12^\circ$ which corresponds to a c -axis spacing of 0.69 nm. Besides the peak at 16.6° similar to GO

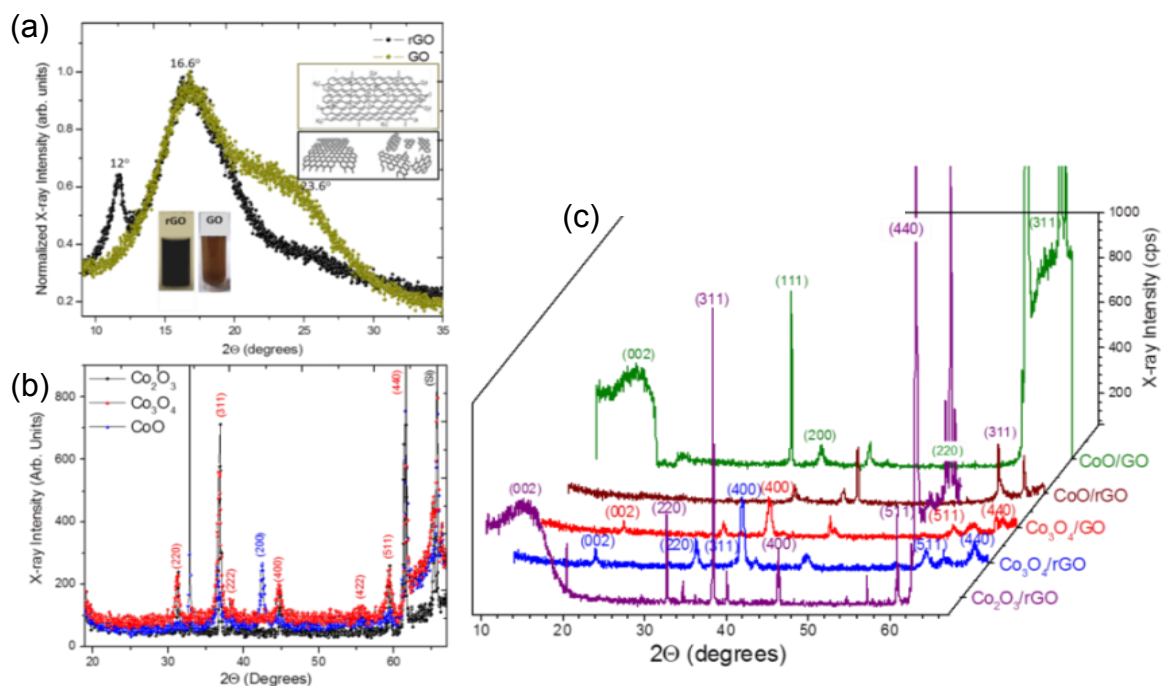


Figure 12. XRD diffractograms for (a) GO and rGO, (b) CoO and Co_3O_4 , and (c) their hybrids, peaks of interest for hybrids are marked with their (hkl) index.

ascribed to the residual carboxyls and hydroxyls groups in rGO, the 16.6° peak is likely induced by a bimodal or multimodal character of the interplanar spacing of rGO. Even though the mechanism of rGO reduction is not yet identified, the reduction may have begun from the edges of GO sheets (relatively more energetic) and continued into the basal planes. During the reduction, parts of the basal planes near the edges are reduced and later snap together due to π - π^* interactions, thus narrowing the interlayer distance. Therefore, the reducing agent, monohydrate hydrazine, is not able to penetrate further into the interior of the rGO flakes, potentially decreasing the degree of reduction, which coincides with *c*-axis spacing of 6.91 Å. All of the XRD peaks (Figs. 12b and 12c) can be indexed with cubic spinel-type Co₃O₄ [JCPDS card No. 78-1970 and JCPDS card no. 43-1003, *a* = 8.08 Å] phase and rock salt periclase CoO (JCPDS card No. 15-0806) phase, including (111), (200), (220), (222), (311), (400), (422), (440), and (511). Other characteristic peaks from possible impurities such as precursors were not detected. The procedure to investigate the crystalline structure of as-prepared nano-/micro- crystallites films of CoO and Co₃O₄ was the Rietveld refinement.⁷³ Some of the peaks at $2\theta = 31.29^\circ$, 36.81° , 59.37° , and 65.27° correspond to the indexed (220), (311), (440) and (511) reflections of the periclase CoO and of the spinel-type Co₃O₄. The sharper peaks indicate high crystallinity with lattice constant of *a* = *b* = *c* = 8.02 Å and *a* = *b* = 4.258 Å based on (220), (311) and (400) planes.⁷⁴ The crystallite size is obtained from XRD analysis using the following Debye-Scherrer equation:⁷⁵

$$L_{hkl} = K\lambda / \beta_{hkl} \cos\theta_{hkl} \quad (6),$$

where L_{hkl} is the crystallite size in nm, λ is the wavelength of Cu K_{α} , β_{hkl} is the full-width at half-maximum, and $K = 0.94$ is the shape or structure constant. Even though the

diffraction peaks of the hybrids are broad and of low intensity, the peak maintain crystalline phases of the components, indicating true high-quality formation of the hybrid composites.

Variation of lattice spacing (d_{hkl} , Å) from Bragg's law and particle size (L_{200} , nm) from Debye-Scherrer formula were determined through analysis of the peak at $2\theta = 31.29^\circ$ for all of the samples along with individual components. Compared to rGO and GO, an increase in lattice spacing ($4.8 \rightarrow 9.0$ Å) and particle size ($2.8 \rightarrow 3.6$ nm) of hybrids is observed. This increase in crystallite size is explained by considering the integration process due to the functional groups present on graphene derivatives and the dangling bonds associated with cobalt oxides, which are related to the cobalt and oxygen defects at the grain boundaries and surface of the nanoparticles. Therefore, these defects favor the linking process, resulting in larger grain or crystallite values. The XRD determines the variation in size of coherent diffracting domain (CDD) since they are smaller than the actual particle sizes, which is the case herein.

Raman spectra of free CoO and Co₃O₄: Raman spectroscopy (RS) is employed to observe the structural features including the precursor phases structure (Figs. 13a and 13c) and the graphene sheets in the hybrid composites (Figs. 13b and 13d). RS of graphene-based systems is well-documented,⁷⁶ and briefly documented for various cobalt oxides;^{77,78,79} however, not of graphene supported hybrids of cobalt oxides. The micro-Raman spectra of free Co₃O₄ and CoO micro-/nanoparticles consist of five characteristic Raman-active peaks at ~ 194.4 (F_{2g}; LO), 482.4 (E_g; TO), 522 (F_{2g}; LO), 618.4 (F_{2g}; TO) and 691.3 (A_{1g}; TO) cm⁻¹ which correspond to skeletal vibrations, in agreement with the bulk cubic CoO and Co₃O₄ phases reported in the literature.^{77,80}

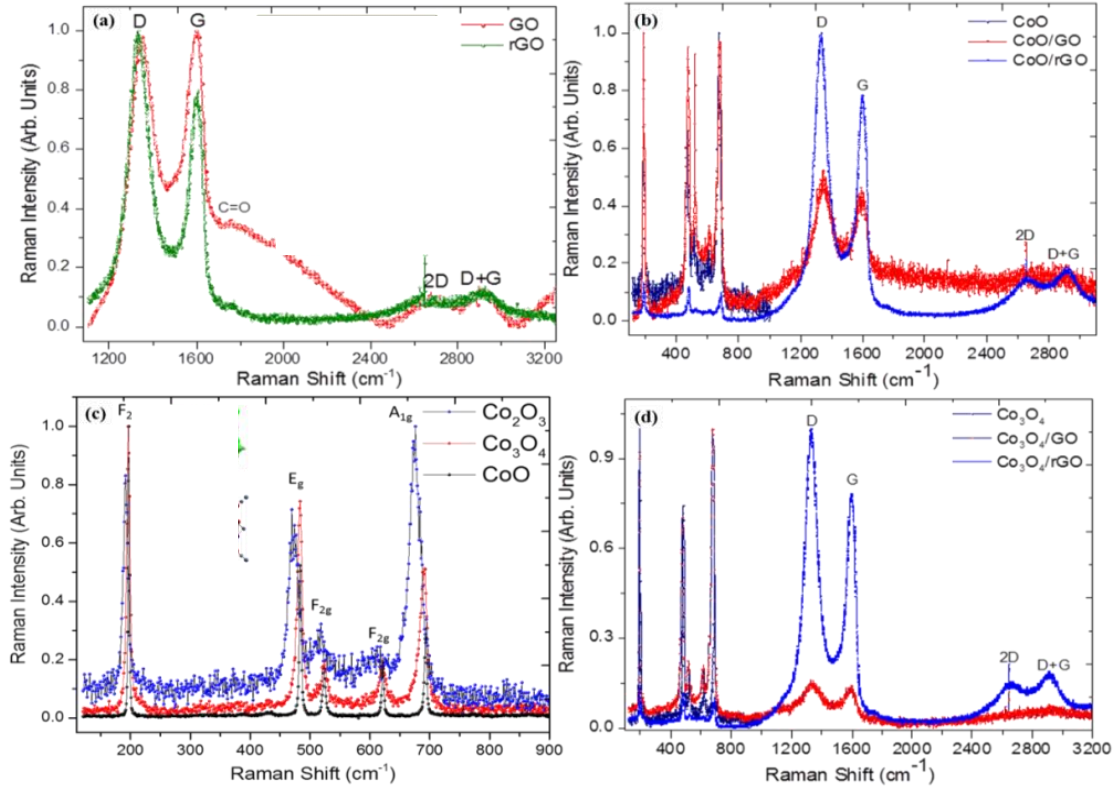


Figure 13. Micro-Raman spectra of (a) GO and rGO, (c) nano-/microscale cobalt oxides CoO, Co₂O₃, Co₃O₄, and (b, c) their corresponding hybrids.

While both the CoO and Co₃O₄ bands are sharp (full-width at half maximum of 4.9, 6.0, 9.5, 7.3, 6.9 cm⁻¹), Co₂O₃ band is rather broad and shifted possibly due to the bonding character. Based on irreducible representations for Co₃O₄, which crystallizes in normal spinel structure Co²⁺(Co³⁺)₂O₄ (space group O_h⁷) with Co²⁺ and Co³⁺ occupying tetrahedral and octahedral sites, respectively, the reduction of the 42-dimensional representation of the vibrational modes at $k = 0$ (zone center phonons) into irreducible representations of the factor group O_h⁷ gives: $\Gamma = A_{1g} + E_g + 3F_{2g} + 5F_{1u} + 2A_{2u} + 2E_u + 5F_{2u}$. The A_{1g}, E_g, and three F_{2g} modes are Raman active. From the five F_{1u} modes four are infrared active and one is an acoustic mode. The remaining 2A_{2u}, 2E_u, and 5F_{2u} modes are inactive. The assignment of the phonon symmetries of optically active

vibrations (both longitudinal; LO and transverse; TO) builds on the results of factor-group analysis of the lattice vibrations of the spinel structure mentioned above.^{81,82} Simple calculations for back scattering from the (111) surface demonstrate that the scattering cross section should not be dependent on the crystal surface rotation around the propagation direction of the incident light.⁸⁰ Moreover, the TO-LO splitting supplies a criterion for the ionic character. The high-frequency peak, A_{1g} , at $\sim 692 \text{ cm}^{-1}$ has been assigned to a vibration that is largely determined by the octahedral cations in the normal spinel, whereas $F_{2g} \sim 522 \text{ cm}^{-1}$ and E_g modes combine the vibrations of tetrahedral and octahedral sites. Furthermore, Co-O lattice vibrations in CoO correspond to distortion vibration of Co-O in an octahedral environment in Co_3O_4 . Among the signals of the CoO Raman spectrum shown in Fig. 13b, the strongest bands lie at 190, 482, and 691 cm^{-1} , the latter may be assigned to Co formed during the spectrum acquisition because of the local heating of the samples. Nevertheless, the absence of additional bands in all of the samples suggest thermal stability. The band at 691 cm^{-1} has a much larger intensity for CoO than for Co_3O_4 film. The 427 cm^{-1} band in the case of CoO appears as a consequence of the formation of a new compound which was identified as metastable Co_2O_3 with a distorted periclase structure, an intermediate formed during the decomposition of CoO to Co_3O_4 or vice versa. Therefore, the peaks at 427 and 180 cm^{-1} can be attributed to the characteristic features of CoO. Interestingly, no similarity exists between the Co spectrum and that of Ref. 79, except some differences between the relative peak heights, however, Co is observed to have the same feature as CoO, which may be a result of having a CoO oxygen-deficient species. For symmetry considerations, although all Raman modes scattered rather strongly, particularly for the 690 cm^{-1} mode,

which is assigned as A_{1g} mode, the stretching mode of Co–O bond is attributed in CoO_6 octahedral, because the structural frameworks of cobalt oxides consist of CoO_6 octahedral units shared by corners and/or edges similar to manganese oxides.^{83,84} In CoO , Raman scattering originates from a collective vibration mode of the CoO_6 octahedron. At lower wavenumbers, the peaks correspond to the deformation modes of the metal–oxygen chain of Co–O–Co in the CoO cubic lattice. Since a cobalt atom is roughly five times heavier than an oxygen atom, the Co–O vibrations are expected to engage primarily the oxygen atoms. The peak at 482.4 cm^{-1} is broad due to smaller crystallite size, while the peak at 690 cm^{-1} is marginally asymmetric likely due to the secondary crystalline phase CoO and/or Co_2O_3 observed in Fig. 13c. The vibrational band located at 482 cm^{-1} corresponds to the vibration of cobalt species ($\text{Co}^{3+}\text{-O}^{2-}$) in the octahedral site of Co_3O_4 . The relative intensity for each vibrational mode is lower potentially owed to the confinement of phonons by some crystal defects induced by Co^{4+} vacancies and oxygen related defect sites, resulting in the decay of phonons and destruction of conservation of phonon momentum. The Raman peak intensity at 620 cm^{-1} tends to fade with smaller particle diameter because the number of surface atoms increases rapidly when the nanoparticle size decreases, having a large number of dangling bonds.

Raman spectra of graphene-supported CoO and Co₃O₄: The optical appearance of the hybrids is highly homogeneous particularly with an irregular amberish dust or blackish surface spotted with dark green islands. From one point to another, the difference in surface composition going is apparent, albeit minimal. The Co_xO_y layer was sufficiently thin that GO and rGO supports were successfully recognized in the

measurement. The first- and second-order Raman spectra of rGO and GO films show two characteristic intense peaks, G band at $\sim 1580 \text{ cm}^{-1}$ and 2D band at $\sim 2670 \text{ cm}^{-1}$, which are assigned to the in-plane vibrational mode (E_{2g} phonon of the C_{sp^2} atoms at the Brillouin zone center, $k \sim 0$) and the intervalley double resonance scattering of two TO phonons around the K-point of the Brillouin zone, respectively. We ascribe the 2D band to signify the second-order or first overtone of the D band. Other relevant features at $\sim 1340 \text{ cm}^{-1}$ are a defect induced peak assigned to the D band activated by intervalley double-resonance Raman process and the D and G combination mode (D+G band) at 2920 cm^{-1} .^{76,85} Commonly, the frequency-integrated intensity ratio of D to G band (I_D/I_G) can provide a semi-quantitative measure of defect concentration in graphitic materials and the size of the sp^2 C domains which is found to increase on the reduction of GO.⁷⁶ For comparative analysis, all of the Raman spectra are normalized with respect to the G band intensity. The sensitivity of Raman analysis of these samples is one of the reasons for the difference between Raman and XRD phase identifications. While the XRD diffractograms revealed the existence of only bulk phases, the Raman spectra allow the identification of local surface cobalt oxides species. The analysis of the Raman spectra is done in terms of D, G and 2D band position (ω_D , ω_G and ω_{2D}), the ratio of D to G (I_D/I_G), G to 2D (I_G/I_{2D}), Co to G (I_{Co}/I_G), as well as 2D versus G band position (ω_{2D} versus ω_G), where the latter is used to determine the nature or type of defects-the results are summarized in Fig. 14. Whereas for GO-based hybrids, the D band varies between $1345\text{-}1325 \text{ cm}^{-1}$ and G band is between $1593\text{-}1581 \text{ cm}^{-1}$, the D band for rGO-based systems is between $1330\text{-}1332 \text{ cm}^{-1}$ and the G band varies approximately between $1605\text{-}1592 \text{ cm}^{-1}$, which is within the spectral resolution. On the other hand, the 2D band

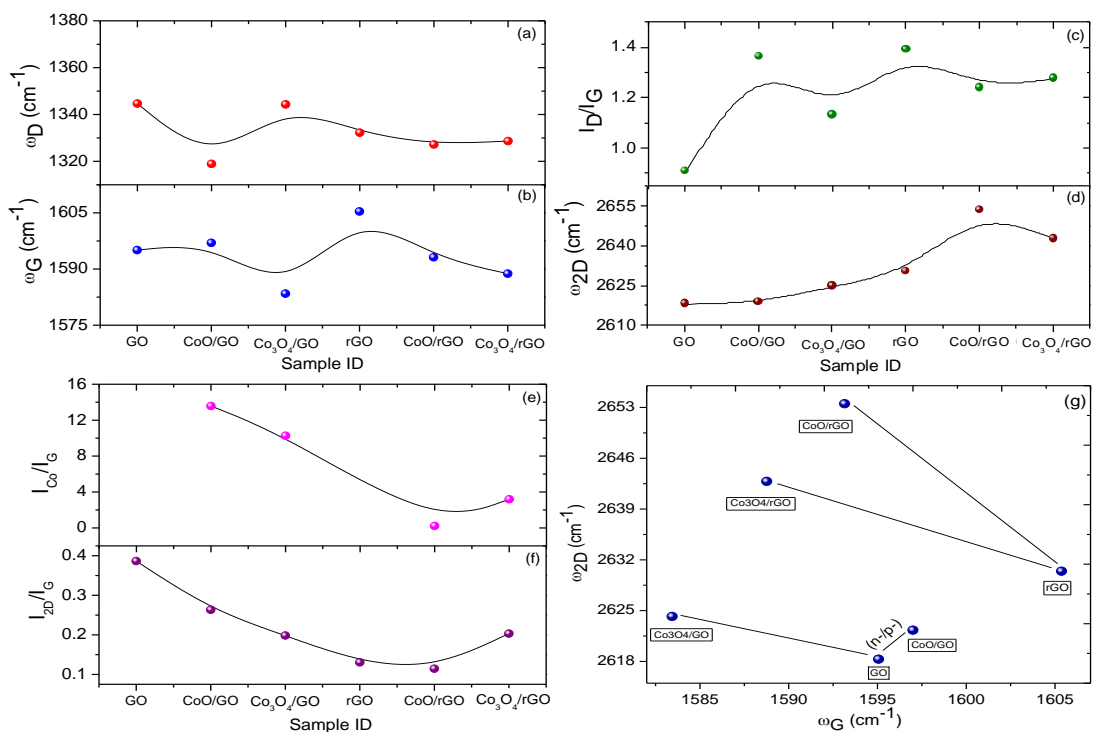


Figure 14. Variation of prominent Raman spectral bands for GO and rGO hybrids with CoO and Co₃O₄ in terms of (a) ω_D , (b) ω_G , (c) I_D/I_G , (d) ω_{2D} , (e) I_{C_0}/I_G , (f) I_{2D}/I_G , and (g) ω_{2D} versus ω_G band determining the defect types [*i.e.* residual or neutral versus charged (*p*- or *n*-type)].

changes rather strongly with cobalt oxides on GO (2630–2617 cm⁻¹) and rGO (2650–2625 cm⁻¹) supports.

The frequency-integrated intensity ratios (I_D/I_G and I_{2D}/I_G) of D and 2D bands with respect to G band display strong dependence with cobalt oxides on GO (0.5–1.5 and 0.1–0.4) and rGO (1.1–1.4 and 0.1–0.3) supports. The I_D/I_G is inversely proportional to the fourth power of the laser energy *i.e.* E_L^{-4} (or, λ_L^4) relation which was previously reported in a Raman study of nanographite.^{85,86} Alternatively, based on Raman scattering theory, calculated matrix elements associated with the double resonance processes of D band indicate a dependence of E_L^{-4} of the intensity for nanographite.⁸⁵

For 2D band, an excitation energy dependence of E_L^{-3} is predicted.⁸⁷ For I_{Co}/I_G , the ratio is 10-15 for most of the GO-based samples, this large value is possibly due to thicker Co area, while for rGO based samples, the ratio has lower values of 0.5-3. We also attempted to determine the nature of defects by plotting the 2D band position with G band position (see Fig. 13g) The defects are of residual or *p*-type for GO-based hybrids, while rGO-based hybrids exhibited *n*-type defects (*i.e.* G band increases and 2D band decreases).⁸⁸

The Raman mapping of hybrid samples is shown as representative examples indicative of the surface or spatial homogeneity, allowing indirect measure of elemental composition (sp^2 C or C rich versus Co-rich) similar to EDS (see Fig. 15). The Raman map is created by taking a collection of spectra point-by-point across the desired region (in Fig. 15, these regions are shown as yellow squares on the optical microscope image). The sharpness and almost uniform intensity maps of D, G and Co related bands (corrected for baseline while generating the maps) contoured at the boundary of graphene sheet nanodomains, nanowalls and layers provide insight regarding the higher degree of crystalline order thus intrinsic nature of the GO, rGO and anchored cobalt oxide nanoparticulates. It should be mentioned that the intensity ratio map of Co peak to G peak (referred to as sp^2 C) offers an avenue to local charge transfer features which are a primary consequence of strong electronic / structural coupling of CoO and Co_3O_4 with functional moieties associated with graphene derivatives. Knowing that Co_3O_4 has the normal-spinel structure $Co^{2+}(Co^{3+})_2O_4$, experimental and theoretical measurements have demonstrated that the three low Miller index planes ($\{100\}$, $\{110\}$ and $\{111\}$) of such metallic oxide particles with fcc structure differ not only in the surface atomic density

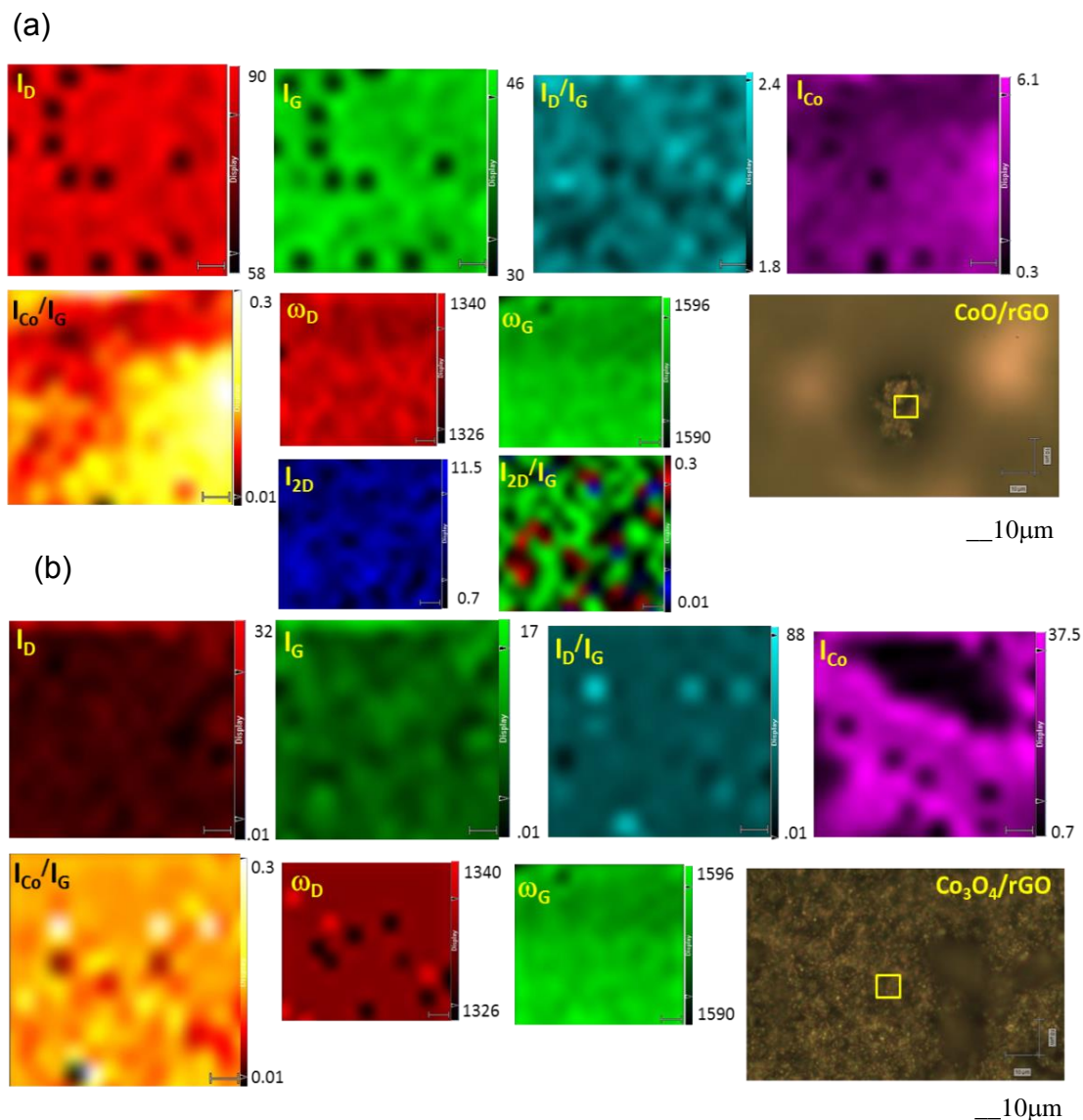


Figure 15. Raman mapping of (a) CoO/rGO and (b) Co₃O₄/rGO in terms of intensity distribution of D, G, 2D and Co bands and their ratio with G band, corresponding optical micrographs, possible surface charge transfer *via* plot of 2D band to G band position for (a) CoO/rGO hybrid. The black regions represent either the substrate (SiO₂) or lower bound as shown with scale bar adjacent.

but also in the electronic structure, geometric bonding and chemical and electrochemical reactivity. As a result, those planes have different surface energies, following the order $\gamma\{111\} < \gamma\{100\} < \gamma\{110\}$, which closely parallels the catalytic activities for CO and CH₄ oxidation.^{89,90,91,92} The catalysis of CO oxidation results as the CO molecule

interacts preferably with the surface Co^{3+} cations, which is the only favorable site for CO adsorption, as confirmed theoretically^{93,94} and revealed experimentally for Co_3O_4 .⁹⁵ The oxidation of the adsorbed CO then occurs by abstracting the surface oxygen that had been coordinated with the Co^{3+} cations. The partially reduced cobalt site, *i.e.* Co^{2+} cation with a neighboring oxygen vacancy, is re-oxidized by a gas-phase oxygen molecule or the oxygen from the water molecules in aqueous electrolyte back to the active Co^{3+} form. Consequently, the surface Co^{3+} cations are considered as the active sites for CO oxidation, while the surface Co^{2+} cations are practically inactive. In the Co_3O_4 crystal structure, the {001} and {111} planes contain only Co^{2+} cations, while the {110} plane is mostly comprised of Co^{3+} cations. This scenario has demonstrated proved by surface differential diffraction studies, concluding that the Co^{3+} cations are present solely on the {110} plane. Similarly, in our own experiment with the $\text{Co}_3\text{O}_4/\text{rGO}$ composite electrode, while the electrochemical activity of the $\text{Co}_3\text{O}_4/\text{rGO}$ (and $\text{Co}_3\text{O}_4/\text{GO}$) composites for CO (carbon monoxide) oxidation are by no means optimized, we are inclined to deduce from our findings that the Co_3O_4 with the predominantly {110} exposed surfaces may have higher electrochemical activity for CO oxidation than the sole six {100} exposed surfaces. In sharp contrast, the Co_3O_4 enclosed by the eight {111} facets on the rGO and GO sheets is expected to exhibit the highest electrochemical activity among the four $\text{Co}_3\text{O}_4/\text{graphene}$ hybrid electrodes. The theoretical prediction is the prevailing electron contribution of Co_{3d} states and other contributions come from O_{2p} oxygen states. The contributions of occupied C_{2p} states at the Fermi level turn out to be smaller by 2 orders of magnitude than the oxygen contributions, being smaller value of 0.008, albeit nonzero. The latter result is consistent with the conductivity of graphene never being

smaller than the minimum value of quantum conductivity unit. Therefore, it is within reason to presume graphene islands can preserve their unique properties in the CoO_x (001)/graphene system. The other implications of this study stem from the direction of nano-electronic and spintronic devices *i.e.* hetero-interfaces of the graphene / (ferromagnetic metal or oxide) instead of nanomagnetic p-type semiconductor or traditional metal. It is ideal for spintronics due to a small spin-orbital interaction as well as a vanishing nuclear magnetic moment of carbon atom.^{96,97}

In addition to spectroscopic studies, I-V measurements were performed to determine two-terminal device resistance R_{2t} and the corresponding σ_{dc} . Qualitatively, graphene derivatives followed quasi-semiconducting behavior and all of the hybrid films followed almost ohmic or linear behavior, showing the higher resistance for $\text{Co}_3\text{O}_4/\text{GO}$ and the lower for $\text{Co}_3\text{O}_4/\text{rGO}$ as anticipated. The σ_{dc} of rGO was higher by around one order of magnitude ($7 \times 10^5 \text{ S}$) than GO ($0.1 \times 10^5 \text{ S}$) and σ_{dc} of both rGO and GO supported hybrids decreased by similar magnitude, as expected.

The following results and discussion correspond to the electrodeposited samples.

Figure 16 shows SEM micrographs at various magnifications of constituents (MLG, CoO and Co_3O_4) and of hybrids (CoO/ErGO, CoO/MLG, $\text{Co}_3\text{O}_4/\text{ErGO}$, $\text{Co}_3\text{O}_4/\text{MLG}$, and CoNP/MLG). As in the case of physically deposited hybrids, electrochemical synthesis yields distinctive cobalt oxide micro/nanoparticles with apparent crystalline facets and similar particle size, agglomerated as observed for CoO (see Fig. 16a). Both ErGO wrinkled sheets and MLG 3-dimensional foam are coated by a homogenous layer of cobalt oxide and cobalt nanoparticles, respectively. Ni foam, allowing for increased surface area for cobalt anchoring and thus for ion adsorption.

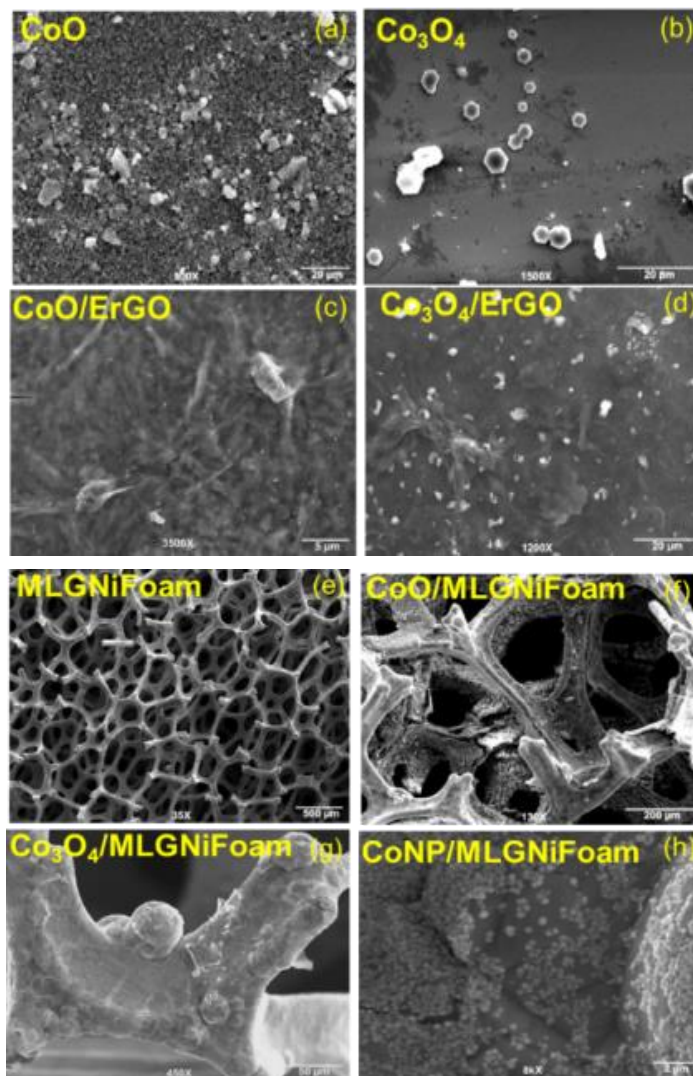


Figure 16. SEM images of (a) CoO and (b) Co₃O₄, ErGO with (c) CoO and (d) Co₃O₄ hybrids, and (e) multilayered graphene (MLG) on Ni foam and hybrids with (f) CoO, (g) Co₃O₄, and (h) CoNP. (Scale bars are shown at the bottom of the images).

For assessing the nanoscale surface morphology, TEM images of the electrodeposited samples were collected (Fig. 17). As physically deposited samples, the cobalt oxide crystallites are apparent for both constituents and hybrids as agglomerated structures. The particle size for cobalt oxides and cobalt nanoparticles alone ranges from

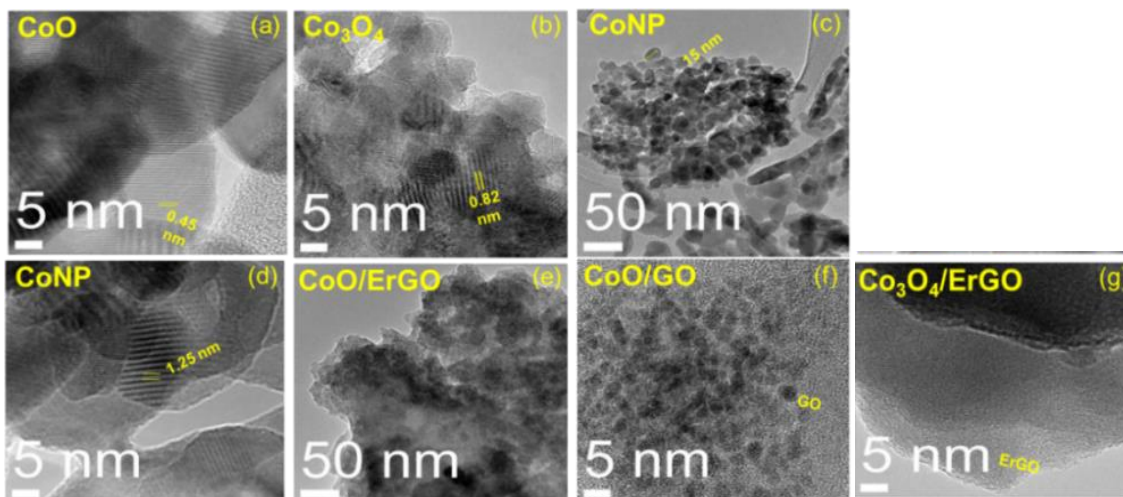


Figure 17. TEM images for CoO, Co₃O₄, and CoNP (a-d), (e) ErGO and (f) GO with CoO, and (g) ErGO with Co₃O₄. (Scale bars are shown at the bottom of the images).

15 nm (CoNP, Fig. 17c) and under. The lattice spacing for CoO is 0.45 nm, corresponding to (111) plane, while for Co₃O₄ crystals is 0.82 nm, attributed to the (311) planes (see Figs. 17a and 17b). In the case of CoNP, the interplanar spacing observed is 1.25 nm. The CoO hybrids in Figs. 17e and 17f and Co₃O₄/ErGO hybrid in Fig. 17g show successful uniform loading of the crystals onto the nanosheets of GO and ErGO. For Co₃O₄/ErGO, the stacking of layers of ErGO is observed at an edge site.

The XRD patterns of Co₃O₄, Co₃O₄/ErGO, Co₃O₄/rGO, and Co₃O₄/MLG are shown in Fig. 18a. Both ErGO and rGO hybrid patterns contain a broad peak at $2\theta = 24.5^\circ$ (002) due to disordered stacking of graphene nanosheets, a shorter peak at $\sim 12^\circ$ attributed to *c*-axis spacing of 0.69 nm, and a peak at 50.66° (004) a feature likely due to a precursor used in the synthesis. The sharper peak at $\sim 12^\circ$ is potentially due to a crystalline form of precursor material remaining in the hybrid. The peak at 26.98° (002) corresponds to multi-layer graphene and the peaks at 44.82° (111) which overlaps the (400) phase of Co₃O₄ and 52.22° (200) corresponds to Ni foam.^{33,98} For the XRD patterns of CoO and CoNP on MLG, the peaks of Ni foam and MLG are observed as in

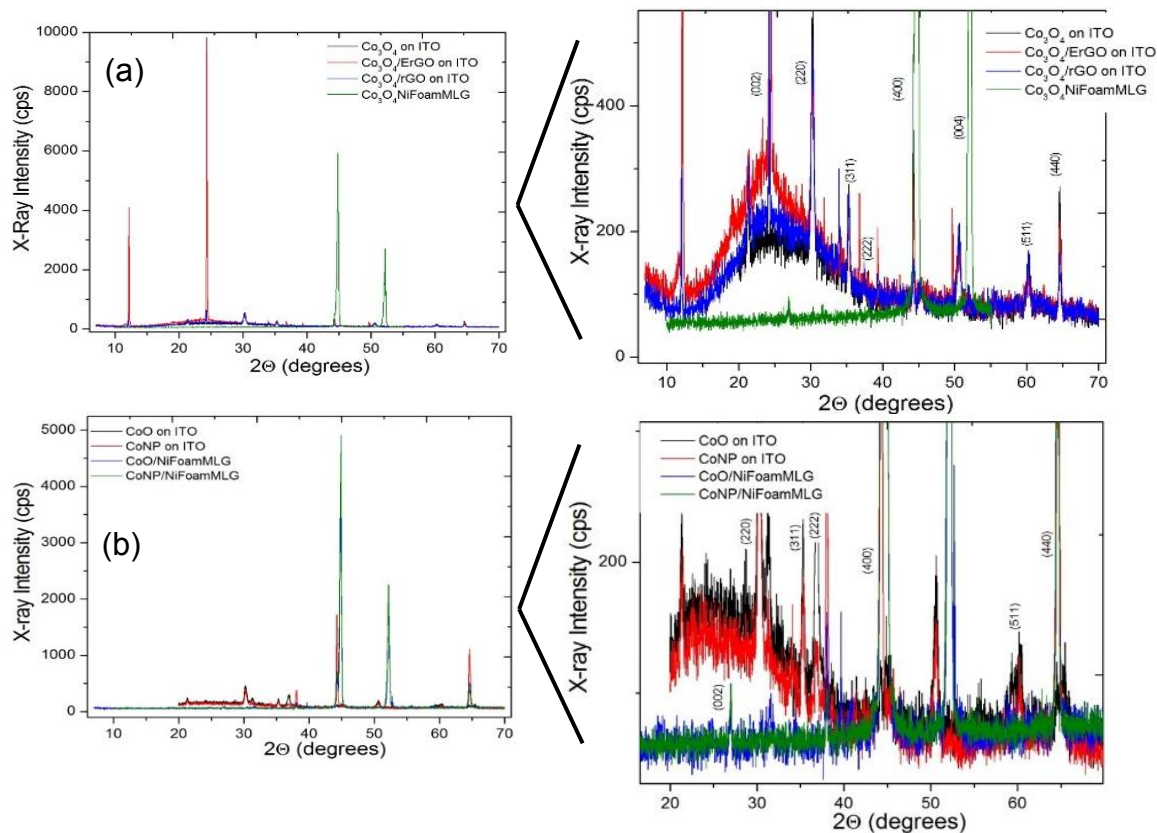


Figure 18. XRD diffractograms with their respective amplifications for (a) Co_3O_4 and corresponding hybrids with graphene based supports on ITO substrate, (b) CoO, CoNP and corresponding hybrids with MLG on Ni foam substrate. The peaks of interest for hybrids are marked with their (hkl) index.

the diffractogram of $\text{Co}_3\text{O}_4/\text{MLG}$ (Fig. 18b). All of the XRD peaks can be indexed with cubic spinel-type Co_3O_4 [JCPDS card No. 78-1970 and JCPDS card no. 43-1003, $a = 8.08 \text{ \AA}$] phase and rock salt periclase CoO (JCPDS card No. 15-0806) phase, and face-centered cubic CoNP (JCPDS card No. 15-806) phase, including (220), (222), (311), (400), (422), (440), and (511). The sharpness of the peaks is indicative of high crystallinity that combined with the features of graphene-based support with cobalt oxide polymorphs and/or cobalt nanoparticles qualitatively confirms the formation of hybrids.

Raman spectra of free Co₃O₄, CoNP, and CoO: The micro-Raman spectra of free CoNP and CoO observed in Fig. 19a contains the five characteristic Raman-active peaks at ~ 193.9 (F_{2g}; LO), 475.8 (E_g; TO), 516.9 (F_{2g}; LO), 615 (F_{2g}; TO), and 678.8 (A_{1g}; TO) cm⁻¹ corresponding to skeletal vibrations. The Co₃O₄ spectrum consists of the similar peaks; however, the E_g, F_{2g}, and A_{1g} peaks are shifted to 458.8 cm⁻¹, 563.0 cm⁻¹, and ~737.0 cm⁻¹ and are broader likely due to crystalline defects. As in the case of CoO and Co₃O₄ physically deposited electrodes, the high-frequency peak, A_{1g}, (678.8 cm⁻¹ for CoO and ~737.0 cm⁻¹ for Co₃O₄) is attributed to a vibration of the octahedral cations in the normal spinel while F_{2g} (~516.9 cm⁻¹ and 563.0 cm⁻¹, respectively) and E_g modes

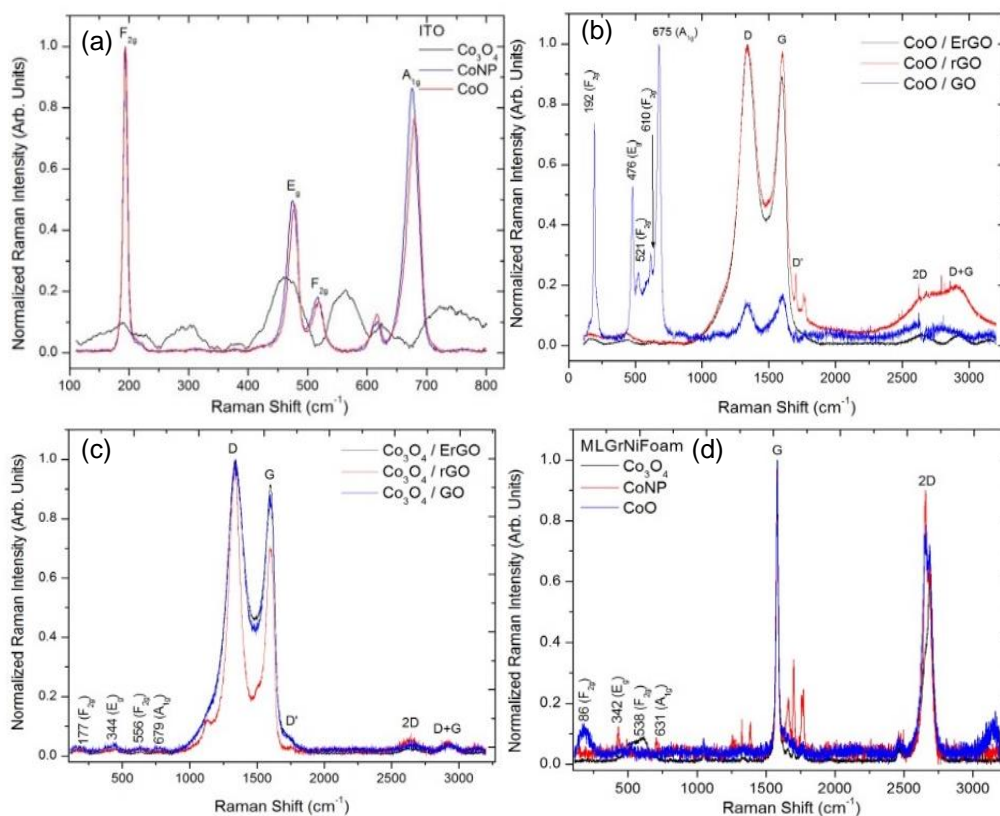


Figure 19. Micro-Raman spectra showing characteristic peaks for (a) cobalt oxides and CoNP, ErGO, rGO, and GO hybrids with nano-/microscale (b) CoO and (c) Co₃O₄, and (d) MLG on Ni foam decorated with Co₃O₄, CoNP, and CoO.

originate from the vibrations of tetrahedral and octahedral sites. Even though CoNP is intended to be solely cobalt integrated, CoNP is an oxygen deficient species in which defective sites may resemble the structure of CoO. The similarity of spectra in CoNP and CoO suggests our cobalt nanoparticulates are organized in fcc, originating similar vibrations for E_g , F_{2g} , and A_{1g} . For Co_3O_4 , the vibration band located at 458.8 cm^{-1} corresponds to the vibration of cobalt species ($Co^{3+}-O^{2-}$) in the octahedral site of Co_3O_4 . As noted previously, each vibrational mode has a lower relative intensity than those of the graphene variants caused by the confinement of phonons by some crystal defects induced by Co^{4+} vacancies and oxygen related defect sites, causing phonons to decay and destroying conservation of phonon momentum.

Raman spectra of graphene-supported Co_3O_4 , CoNP, and CoO: The Raman spectra of the graphene-supported hybrids is observed in Figs. 19b, 19c, and 19d. For Co_3O_4 and CoO hybrids (Figs. 19b and 19c), the ErGO, rGO, and GO films show the two characteristic intense peaks, G band at $\sim 1580\text{ cm}^{-1}$ and 2D band at $\sim 2670\text{ cm}^{-1}$. The additional features include D band at $\sim 1340\text{ cm}^{-1}$, D' band at $\sim 1750\text{ cm}^{-1}$, and D+G band at $\sim 2910\text{ cm}^{-1}$. D' corresponds to defect scattering similar to D.⁹⁹ The multi-layered graphene on Ni foam supported hybrids spectra also contain the characteristic G band at 1535.4 cm^{-1} and the 2D band at $\sim 2642.4\text{ cm}^{-1}$, where the splitting of 2D is identified as a result of the layered character of graphene. The additional unlabeled peaks can be attributed to nickel and/or nickel oxides from the substrate. Even though the cobalt related peaks are only prominent in the CoO/GO and CoNP/MLG spectra, they are present for all hybrids at a lower relative intensity as a consequence of crystalline defects. Since cobalt polymorphs and cobalt nanoparticles are more stable than

graphene-based supports at higher temperatures, the annealing process of the hybrids which exposes the features of cobalt was limited and thus yielded weaker bands. As for physically absorbed samples, all of the Raman spectra are normalized with respect to the highest peak.

The subsequent results and discussion belong to the hydrothermally synthesized samples

SEM and TEM images were taken to observe the micro and nanoscale surface morphology of hydrothermally synthesized Co_3O_4 -graphene hybrids (Fig. 20). The structural similarity of $\text{Co}_3\text{O}_4/\text{GO}$ and $\text{Co}_3\text{O}_4/\text{rGO}$ caused by the hydrothermal reduction of GO is observed in the SEM images; however, as shown in Fig. 20a, some of the sheet character of GO is conserved after the treatment. Aggregation of Co_3O_4 crystals on the surface of rGO and GO is evident in the SEM micrographs while the TEM images reveal well dispersed crystals (Fig. 20b). The Co_3O_4 crystals are not visible in the TEM image for the rGO hybrid owing to the folding/crumpling of the sheets covering the crystallites

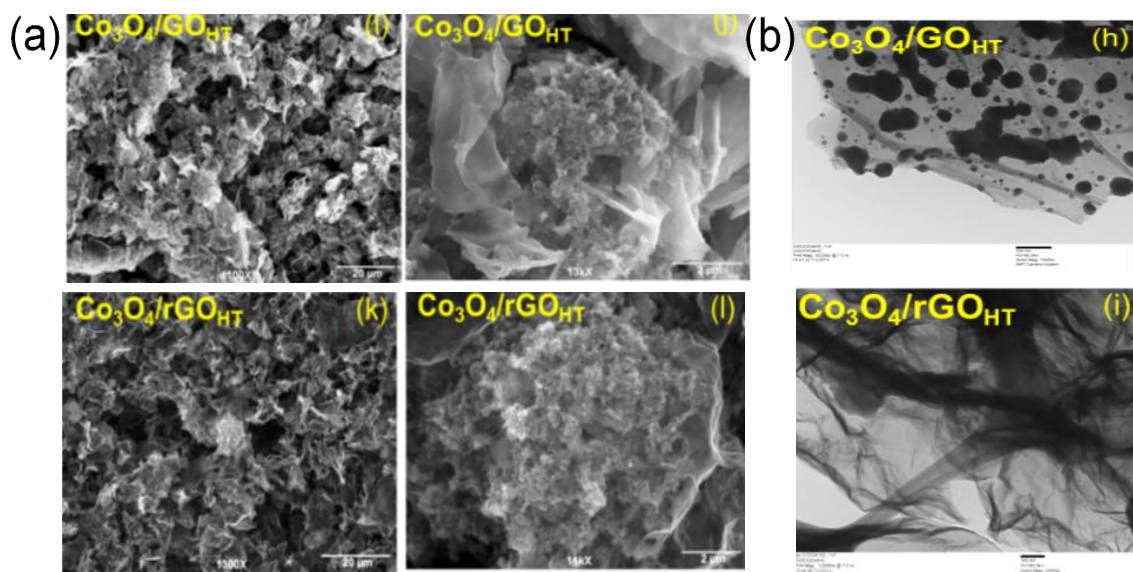


Figure 20. SEM (a) and TEM (b) images of hydrothermally synthesized GO and rGO with Co_3O_4 . (Scale bars are shown at the bottom of the images).

as expected from the synthesis. Even though visually the particles are not perceived, XRD and Raman spectra reveal characteristic behavior of this hybrid, corroborating successful synthesis.

Fig. 21a shows the XRD patterns of $\text{Co}_3\text{O}_4/\text{GO}$ and $\text{Co}_3\text{O}_4/\text{rGO}$ hydrothermally synthesized and deposited on standard steel substrate. As observed in the physical and electrochemical deposited hybrids, the broad reflection at $2\theta = 24.5^\circ$ is present for both GO and rGO hybrids. The close resemblance in the data of GO and rGO can be attributed to the reduction of GO during hydrothermal treatment. The peaks (220), (222), (400), and (440) relate to cubic spinel-type Co_3O_4 as previously observed. The sharp peak around $\sim 12^\circ$ is not evident as in the case of electrodeposited hybrids which may be the result of the heat exposure cleaning the hybrid of precursors.

As observed in the XRD, the micro-Raman spectra for both rGO and GO supported Co_3O_4 have analogous features (Fig. 21b). Similar to the physical and electrochemical deposited samples, the characteristic G band at 1589 cm^{-1} and 2D $\sim 2640\text{ cm}^{-1}$ are present for both hybrids as well as the additional bands (D band 1333.2 cm^{-1} and D+G at $\sim 2920\text{ cm}^{-1}$). Even though the related peaks of Co_3O_4 are more distinctive for

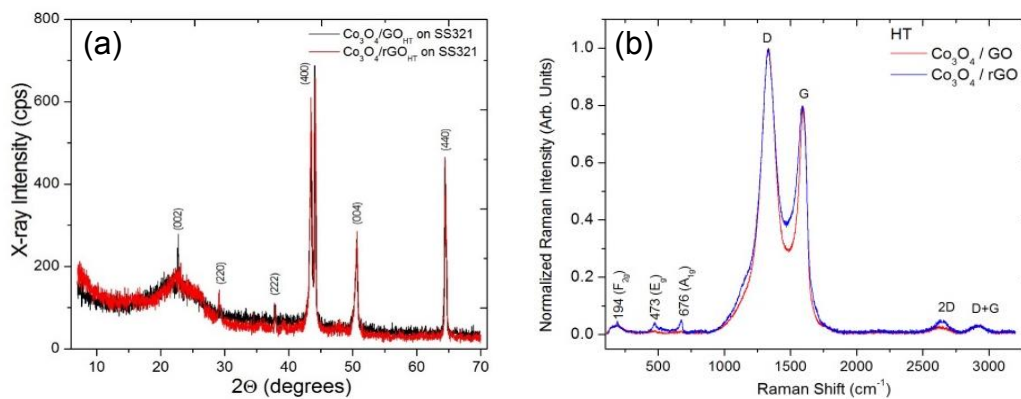


Figure 21. (a) XRD diffractograms and (b) micro-Raman spectra of GO and rGO hydrothermally synthesized hybrids with Co_3O_4 .

the hydrothermally synthesized samples, their low relative intensity can be the result of the 3-dimensional character of the hybrid embedding the Co-nano/micro particulates within the architecture where the Raman laser cannot access them. The main vibration modes for Co_3O_4 [CoO and Co_2O_3] are distinctive to F_{2g} at 194 cm^{-1} , E_{2g} at 473 cm^{-1} , and A_{1g} at 676 cm^{-1} . Other peaks due to potential impurities are not present in either spectrum.

2.4 Conclusion

All of these results confirm successful loading of cobalt oxide polymorphs and cobalt nanoparticles on graphene derivatives by various synthetic approaches. SEM provided a macroscale surface morphology of GO and rGO that revealed the nanosheets and the nano-/micro- particles of CoO , Co_3O_4 , and CoNP well-dispersed within the sheets/vertical walls of GO and rGO. TEM allowed the nanoscale observation of the surface morphology of the hybrids and facilitated the calculation of GO sheet thickness and particle size distribution along with SAED patterns depicting GO (rGO) rings and diffraction spots of polycrystalline CoO and Co_3O_4 . XRD provided the average structure of the hybrids by showing the characteristic peaks of cobalt oxide polymorphs, CoNP, and GO (and rGO). RS contained characteristic GO (and rGO) and CoO (Co_3O_4 and CoNP) Raman bands in hybrids confirming the formation of tailored interfaces crucial for applied electrochemistry and provided local charge transfer due to physical (or chemical) adsorption of cobalt oxide onto graphene derivative support. Raman maps also verified the hybrid formation by determining the distribution of C and Co.

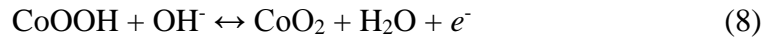
Chapter 3: Electrochemical Properties of Graphene-based Hybrid Nanomaterials.

In Chapter 3, the electrochemical properties were obtained, such as gravimetric capacitance and diffusion coefficient, from the previously synthesized hybrids (Chapter 2) using cyclic voltammetry. In addition, relevant circuit elements were deduced from fitting Nyquist plots obtained through electrochemical impedance spectroscopy. Finally, durability was assessed by chronopotentiometry.⁶⁸ To further gain insights into the physical/chemical processes at the electrode/electrolyte interfaces, we performed an advanced electrochemistry namely, scanning electrochemical microscopy (SECM) in two separate modes: probe approach and imaging mode in addition to cyclic voltammetry with microelectrode configuration.

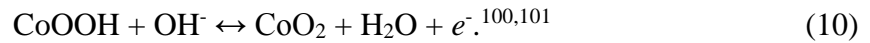
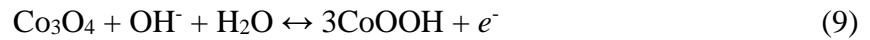
3.1 Results and Discussion

Cyclic Voltammetry

Figure 22 shows cyclic voltammetry (CV) curves with current as a function of potential in 1M KOH. The potential window ranged between -0.2 V and 1V or 0.8 V with respect to the electrochemical behavior of the hybrid. While no redox peaks were observed in the case of CoO and Co₃O₄, clear redox pairs occurred around -0.15 V/0.2 V (Co³⁺ ↔ Co²⁺) and 0.3V/0.4 V (Co⁴⁺ ↔ Co³⁺) for all hybrids, following the respective faradaic reactions



and



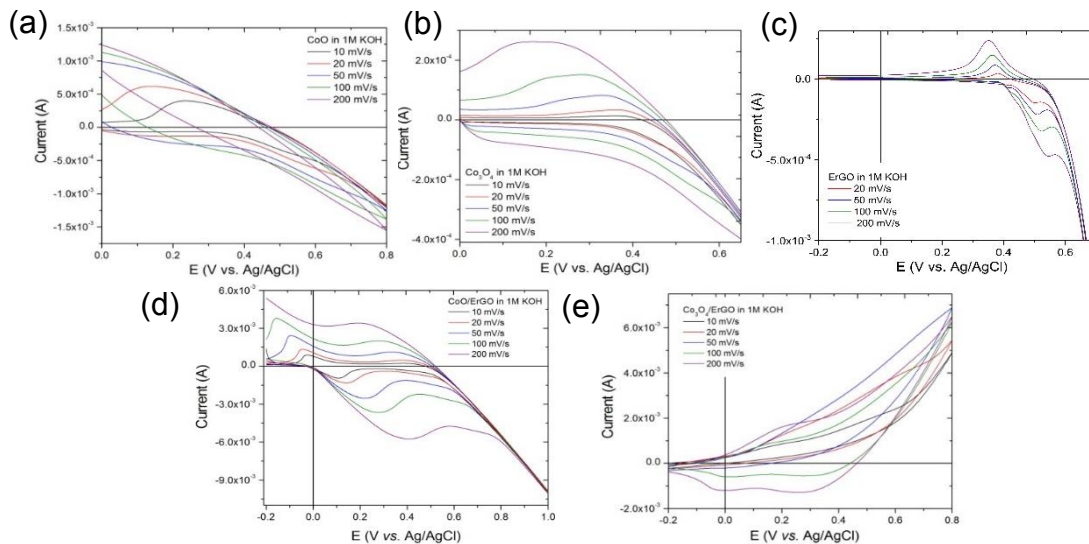


Figure 22. Cyclic voltammograms for representative constituents (a) CoO, (b) Co₃O₄, and (c) ErGO and their corresponding (d) CoO/ErGO and (e) Co₃O₄/ErGO hybrids for scan rates 10, 20, 50, 100, 200 mV/s in 1 M KOH.

The curves corresponding to the representative ErGO hybrids are dominated by the pseudocapacitive behavior of the metal oxides while preserving quasi-rectangular features characteristic of the double-layer capacitance of ErGO (Figs. 22c-22e). Overall, the physically deposited hybrids had less distinctive redox peaks, and most of them were easily degraded from the ITO substrate while all electrodeposited and hydrothermally synthesized hybrids withstood the electrolyte under applied potential. For electrodeposited and hydrothermally prepared electrodes, the coating of relatively thin films followed with low-temperature annealing could explain the strong attachment between the substrate and the material.

From the CV curves, the values for current (anodic and cathodic) were collected where the electrochemical behavior of the hybrid resembled an ideal supercapacitor. The resulting current average for each composite was plotted as a function of the square root

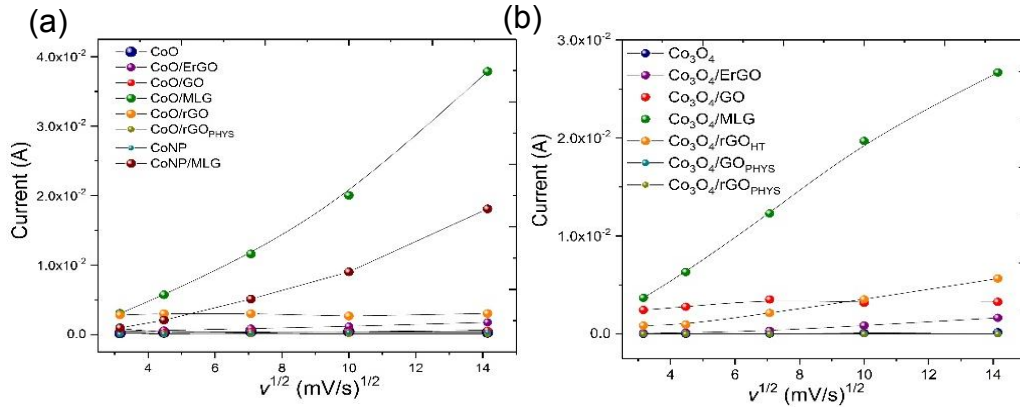


Figure 23. CV analyses in the form of current as a function of square root of scan rate for (a) CoO/graphene and (b) Co₃O₄/graphene hybrids.

of scan rate (Fig. 23). The quasi-linear behavior characteristic of heterogeneous electrodes obeys the Randles-Sevcik equation for quasi-reversible processes

$$i_p = 2.68 \times 10^5 \times \sqrt{n^3 A \sqrt{D} C \sqrt{v}} \quad (11),$$

where i_p is peak current, n is the number of electrons transferred per mole, A is the area of the electrode, D is the diffusion coefficient, C is the electrolyte concentration, and v is the scan rate). From fitting the results with the Eq. 11, the diffusion coefficients were determined, ranging between 4×10^{-8} - 6×10^{-6} m² s⁻¹ and following the order CoO/MLG < Co₃O₄/MLG < Co₃O₄/rGO_{HT} < CoO/ErGO.

Specific gravimetric capacitance (C_s) was also calculated by dividing the peak current with the mass of the material, m , and the scan rate

$$C_s = i_p \times m^{-1} \times v^{-1} \quad (12).$$

Higher values of C_s are indicative of efficient charging (more charge/energy per applied potential). The corresponding values were plotted with respect to scan rate as shown in Fig. 24. All hybrids followed a decreasing trend of C_s with increasing scan rate.

Maximum values of C_s were observed for CoO/ErGO (450 F/g), CoO/MLG (300 F/g),

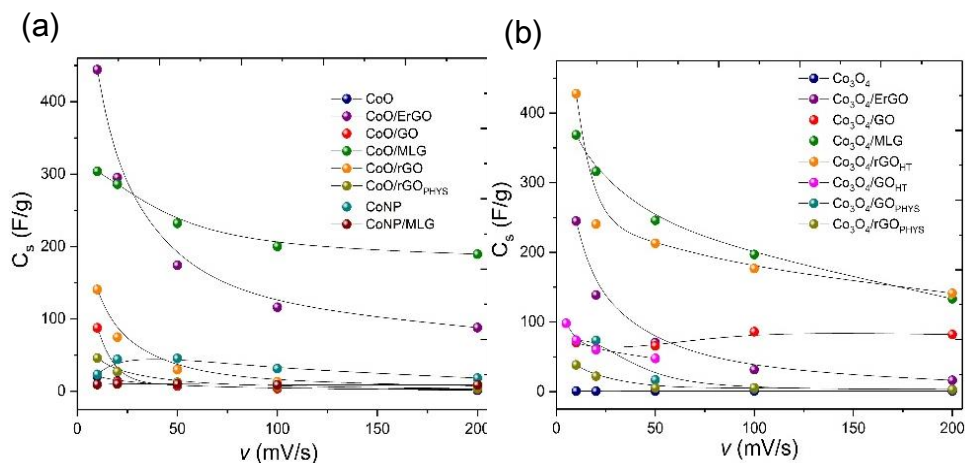


Figure 24. CV analyses in terms of gravimetric capacitance as a function of scan rate for (a) CoO/graphene and (b) Co₃O₄/graphene hybrids.

Co₃O₄/rGO_{HT} (425 F/g), and Co₃O₄/MLG (375 F/g). In the case of Co₃O₄/rGO_{HT}, the higher specific capacitance could be attributed to the 3-dimensional blend obtained through hydrothermal synthesis which contains Co₃O₄ micro/nano crystallites on the surface and throughout the structure that increase the specific capacitance. Similarly, the micro-sized CoO crystals loaded and distributed on the sheets of ErGO result in higher specific capacitance. For the grid-like structure of MLG on Ni foam, the holes facilitate mass transport hence the construction of a double layer by ion absorption while the cobalt oxide crystals allow energy storage by reduction/oxidation of Co²⁺ from/to Co³⁺ and Co³⁺ from/to Co⁴⁺. Thus, the combination of these two types of materials showed enhanced performance in terms of specific capacitance due to both their physical (morphology) and chemical (bonding/interaction between defect and/or functional groups of graphene variants and cobalt oxides) properties.

Impedance Spectroscopy

Electrochemical impedance spectroscopy (EIS) data was collected and analyzed to determine additional parameters to those obtained through CV analysis. EIS involves

applying a small ac potential monitoring the impedance of the system (Z) for a wide range of frequencies ($Z(\omega)$, where ω is frequency). The Nyquist plots (Figs. 25a and 25b) showing the imaginary component of Z ($Z''(\omega)$) vs. the real component of Z ($Z'(\omega)$) contain a high frequency region (semicircle related to kinetics) and a low frequency region (line related to mass transfer). These features may arise due to the contribution from solution resistance, R_s , and Warburg impedance, Z_w , relative to charge-transfer resistance, R_{ct} , kinetically allowing the system to be continually available for mass transfer.⁴⁸ However, the trend of $\text{Co}_3\text{O}_4/\text{rGO}_{\text{HT}}$, for instance, showed more contribution from R_{ct} , having a clearer semicircle and a lack of linearity which could indicate that the system is kinetically slow and has a small frequency window for mass transfer.

Using the RC circuit in Fig. 25 and equivalent circuits with more complex forms, data simulations were generated with in-built digital simulation software with the electrochemical workstation that resemble the experimental behavior of Z . From the simulation, circuit elements including solution resistance (R_s), double-layer capacitance (C_{dl}), Z_w , and R_{ct} were obtained and are summarized in Table 2. These parameters

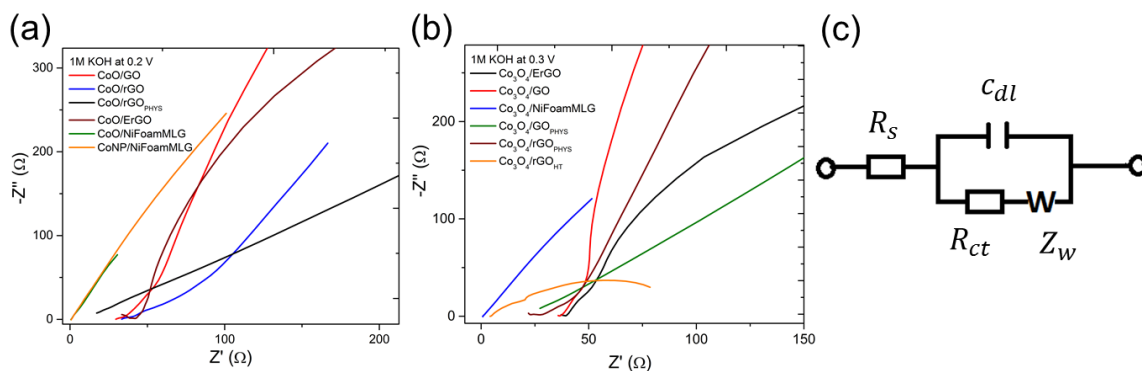


Figure 25. Nyquist plots ($-Z''$ vs. Z') for (a) CoO and CoNP and for (b) Co_3O_4 based hybrids, and (c) the Randles' circuit with its corresponding elements.

derived from the simulations for Co₃O₄/rGO_{PHYS}, Co₃O₄/MLG, CoNP/MLG, CoO/GO, and CoO/MLG had significant contributions from R_s and Z_w while for both CoO/rGO and Co₃O₄/ErGO the contribution was mostly attributed to R_{ct}. The rest of the samples had relatively high values of R_{ct}, coupled with large values of R_s. Furthermore, C_{dl} values were outstandingly high, ranging from 4.3 × 10⁴ μF for CoO/MLG to 1.99 × 10⁻¹ μF Co₃O₄/GO for a working area of approximately 3 cm². The low error values validate the integrity of the data (within 10% discrepancy).

Table 2. Circuit elements, solution's resistance-R_s, charge-transfer resistance-R_{ct}, double-layer capacitance-C_{dl}, and Warburg impedance-Z_w, from ac impedance simulation and fitting.

Synthesis/ Fabrication	Sample	R _s (Ω)	R _{ct} (Ω)	C _{dl} (F)	Z _w (Ω)	Error (%)
Physical	Co ₃ O ₄ /GO	26.76	0.1012	1.985E-07	9.992E-05	7
	Co ₃ O ₄ /rGO	22.88	0.001	0.01256	0.001984	6
	CoO/rGO	5.76	0.001	0.0137	0.0001759	5
Electro-deposition	Co ₃ O ₄ /ErGO	39.42	596.2	0.004587	0.00427	7
	Co ₃ O ₄ /GO	37.09	0.001	3.864E-03	0.0005801	4
	Co ₃ O ₄ /MLG	0.7847	0.002956	1.429E-02	0.1989	10
	CoNP/MLG	0.8013	0.001	3.692E-02	0.009382	11
	CoO/ErGO	30.7	9.417	3.664E-07	0.05236	3
	CoO/GO	30.1	0.0003825	9.672E-04	0.006341	3
	CoO/MLG	0.6314	0.02996	4.280E-02	0.1643	13
	CoO/rGO	10.39	25.83	1.825E-02	0.01156	2

In addition, low-frequency capacitance, C_{lf}, and the imaginary component of capacitance, C''(ω) were determined from EIS. C_{lf} was obtained following the equation

$$\frac{1}{C_{lf}} = \frac{Z''(\omega)}{1/(\omega)},$$

peaking for CoO/MLG, CoO/ErGO, Co₃O₄/rGO_{HT}, and Co₃O₄/ErGO (Figs.

26a and 26b), in agreement with the results from CV analysis, showing overall improved

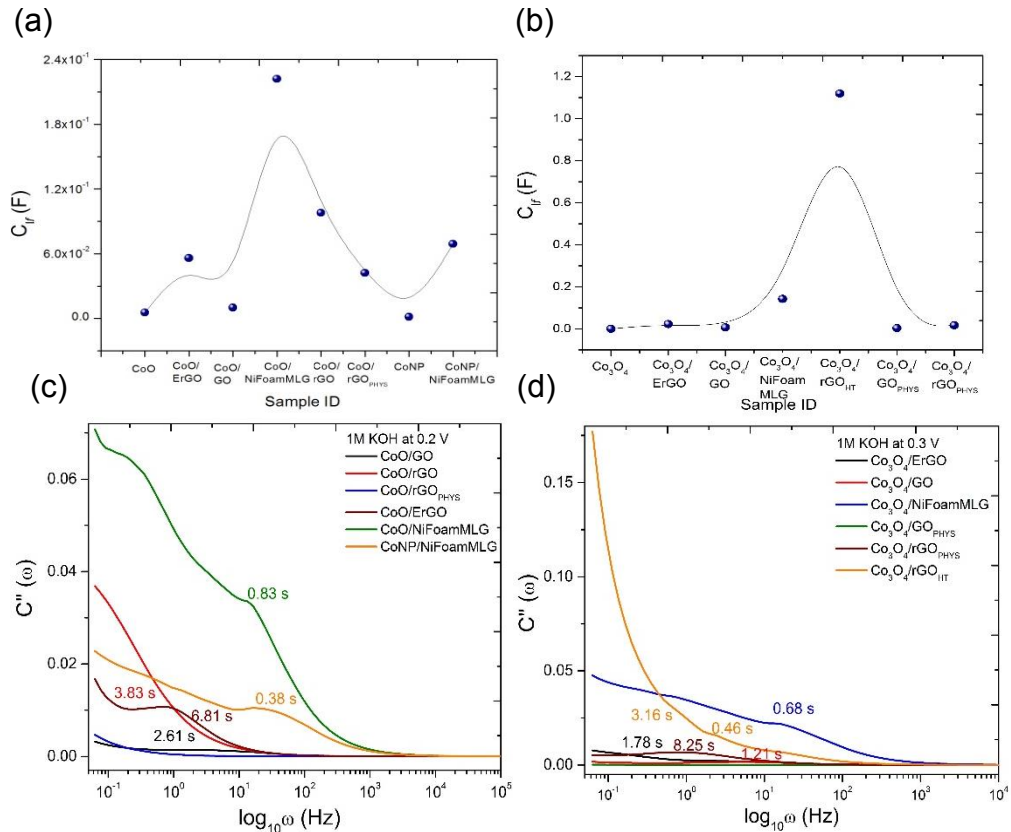


Figure 26. C'' values for (a) CoO and CoNP and (b) Co_3O_4 hybrids. $C''(\omega)$ vs. logarithm of frequency showing the time response for charging-discharging of graphene variants with (c) CoO and (d) Co_3O_4 .

performance of cobalt oxides in the presence of a graphene variant. Similarly, the imaginary component of capacitance, $C''(\omega)$, was calculated through the relation

$$C''(\omega) = -\frac{Z'(\omega)}{\omega|Z(\omega)|^2}.$$

The features of $C''(\omega)$ as a function of the logarithm of frequency

correspond to time-response/charge-discharge time (Figs. 26c and 26d). While some

hybrid electrodes had relatively large charging-discharging times (i.e. physically

deposited $\text{Co}_3\text{O}_4/\text{rGO}_{\text{PHYS}}$, 8.25 s), the times for most hybrids fell between 0.38 s and 4

s, neighboring the optimal value of 0.1 s.

Chronopotentiometry

Chronopotentiometry was performed to assess the cyclability of the electrodes by monitoring the charge-discharge cycling (V-t) for an applied current and to calculate C_s . Figure 27 shows the V-t profiles for representative CoNP/MLG sample, demonstrating stability under applied current for a total of 110 cycles. In the case of both physically and electrochemically deposited GO based hybrids, cyclability was considerably less consistent for the different currents, likely due to the affinity of GO for water which increases the solubility of the sample in the electrolyte and may also facilitate detachment of the material from the substrate. The latter behavior could also occur for thick samples like in the case of CoO/ErGO for which the material undergoes slow “peeling” from the ITO with prolonged exposure to the electrolyte. Despite probable loosening of the material, all samples stably cycled for at least two currents, indicating durability, namely rGO and MLG based hybrids. From the V-t profiles, C_s was calculated for each current using the relation

$$C_s = \frac{i \times \Delta t}{\Delta V} \quad (13),$$

where Δt corresponds to the change in time and ΔV to the change in potential for

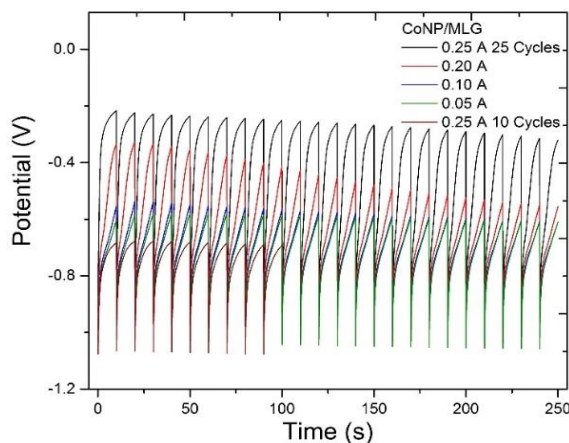


Figure 27. Charge-discharge profiles of representative CoNP/MLG hybrid for 0.25 A g^{-1} , 0.20 A g^{-1} , 0.10 A g^{-1} , and 0.05 A g^{-1} .

discharge current. The largest values of C_s were found for $\text{Co}_3\text{O}_4/\text{rGO}_{\text{PHYS}}$ for all applied currents while the lowest values were shared between CoO/ErGO for 0.25 A g^{-1} and 0.20 A g^{-1} and CoNP/MLG for 0.10 A g^{-1} and 0.05 A g^{-1} as summarized in Table 3. The C_s values for the rest of the hybrids followed the expected decreasing trend with decreasing applied current.

Table 3. Summary of maximum and minimum C_s values obtained from galvanostatic measurements

Applied Current (A g^{-1}) / Sample ID	0.25 ($C_s, \text{F g}^{-1}$)	0.20 ($C_s, \text{F g}^{-1}$)	0.10 ($C_s, \text{F g}^{-1}$)	0.05 ($C_s, \text{F g}^{-1}$)
$\text{Co}_3\text{O}_4/\text{rGO}_{\text{PHYS}}$	81.6	81	42.9	22.7
CoNP/MLG			2.34	1.32

Scanning Electrochemical Microscopy

To gain insights into the storing mechanisms and physical/chemical processes at the electrode/electrolyte interface, scanning electrochemical microscopy (SECM) was used in two modes: probe approach, which probes the nature of the substrate, and imaging mode, which measures the electrochemical behavior at the electrode/electrolyte interface.

Experimental Setup

Since the hybrids were deposited on ITO (only conductive on the deposited side), copper wire was placed at the initial site of deposition and fixed with conductive silver paste to ensure contact. The resulting electrodes were dried under a lamp at $\sim 50^\circ\text{C}$ for 10 minutes, followed by air drying, thus avoiding complete dehydration of the silver paste. The hybrids were then mounted on the SECM stage, and the custom three-

electrode electrochemical cell was fixed exposing a circular area (5 mm diameter) of the sample. The experiments were performed using the tip as the first working electrode, the ITO substrate as second working electrode, Ag/AgCl reference electrode, and platinum counter electrode.

Probe Approach

Similar to atomic force microscopy, the probe approach uses a tip that comes near (in the order micrometers) the surface of the substrate and interacts with it. However, the interaction is facilitated through a redox mediator rather than Van der Waals forces. The mediator creates a redox cycle (reaction) between the tip and the material in study. Thus, depending on the nature of the substrate, the cycle is stimulated (conductive material) or suppressed (insulating material). For all of the hybrid materials, it followed tip current- i_T larger than steady state current- $i_{T,\infty}$ ($i_T > i_{T,\infty}$), exhibiting a ratio of i_T to $i_{T,\infty}$ larger than 1 with respect to the normalized distance (Fig. 28), demonstrating conductive character. In addition, probe approach curves obeyed the equation

$$\frac{i_T}{i_{T,\infty}} = \frac{1}{K_1 + \frac{K_2}{L} + K_3 * e^{-K_4/L}} \quad (14),$$

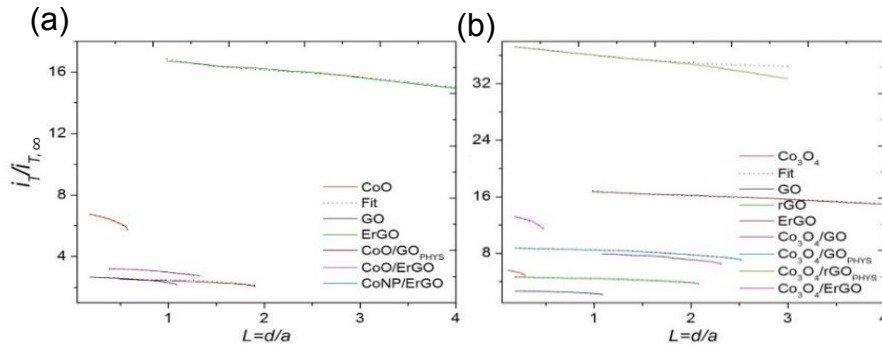


Figure 28. Probe approach curves including experimental (solid) and fitting (dashed) for graphene based hybrids with (a) CoO and (b) Co₃O₄.

where K_1 is the one electron heterogeneous rate constant, K_2 is the multi-electron rate constant, and K_3 and K_4 are fitting parameters describing more complex convoluted processes relate to charge transfer and mass transport. By fitting the probe approach with this equation, K_1 through K_4 were obtained and are summarized in Table 4.

Table 4. Summary of fitting parameters the one electron heterogeneous rate constant- K_1 , the multi-electron rate constant- K_2 , and fitting parameters describing more complex convoluted processes relate to charge transfer and mass transport- K_3 and K_4 from probe approach of various cobalt oxide constituents and cobalt oxide/graphene hybrids.

Sample ID	K_1	K_2	K_3	K_4
Co ₃ O ₄	1.13526	-5.26472	2.29E+14	583.284
Co ₃ O ₄ /GO	1.16017	-5.81842	1.50E+14	600.26827
Co ₃ O ₄ /GO _{PHYS}	1.3043	-7.81377	3.28E+12	544.97382
Co ₃ O ₄ /rGO _{PHYS}	1.43038	-9.7527	7.37E+14	612.3436
Co ₃ O ₄ /ErGO	1.55276	-11.54524	4.19E+14	602.68102
CoO	0.96945	-0.86143	8.58E+02	96.74951
CoO/ErGO	0.87897	-0.56885	20.30655	64.31714
CoO/GO _{PHYS}	1.11866	-1.72954	5.77E+08	156.52439

Imaging Mode

Using SECM, the electrochemical reactivity of a local region of the electrode was probed, generating areal scans that were plotted as two- and three-dimensional maps as shown in Fig. 29. The constituents of representative ErGO hybrids evidenced some reactivity featured through the broad ridges and valleys (Figs. 29a and 29b) and highly electroactive localized sites also called hot spots (Figs. 29b and 29c). The topographical features of the hybrids integrate those of their constituents, visually confirming their combination and the successful distribution of electroactive sites. Compared to the constituents, CoO and Co₃O₄ when coupled with ErGO showed an enhancement of the

reactivity through a high current response on the order of 10 A and 10^2 A. The peaking values for the hybrids were comparable to ErGO, demonstrating that the electrochemical

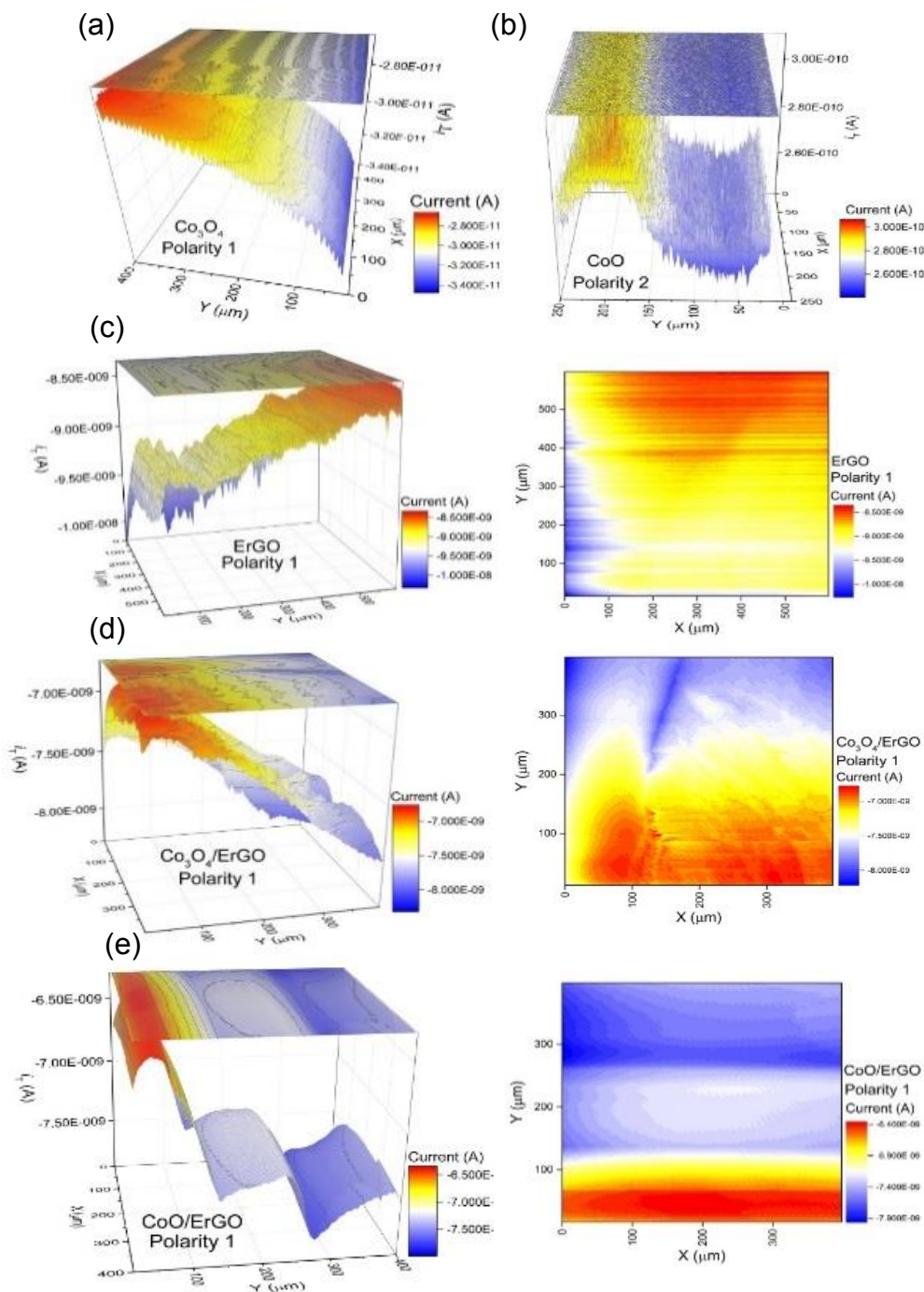


Figure 29. Two- and three-dimensional areal scans of representative (a) Co_3O_4 , (b) CoO , (c) ErGO , and their corresponding (d) Co_3O_4 and (e) CoO hybrids.

reactivity of the hybrids was improved relative to the cobalt oxide constituents. This behavior highlights the importance of ErGO as the physical (supporting network of the crystallites) and chemical (available structural defects/functional groups to serve as a chemical bridge with cobalt oxide and/or as an electroactive site) support.

Electrocatalytic and Sensing Applications

In addition to collecting different properties of the hybrids, two other applications were explored, demonstrating the potential of these materials as catalysts for oxygen reduction-reaction (ORR) and enzymeless glucose sensing. The ORR as the primary reaction for fuel cells requires catalysts that can compete with the current platinum electrode which is scarce and expensive. Therefore, the hybrids were subject to cycling using CV to observe their *i*-*V* response (Fig. 30).

Distinctive redox peaks for representative CoNP/MLG, CoO/ErGO, and

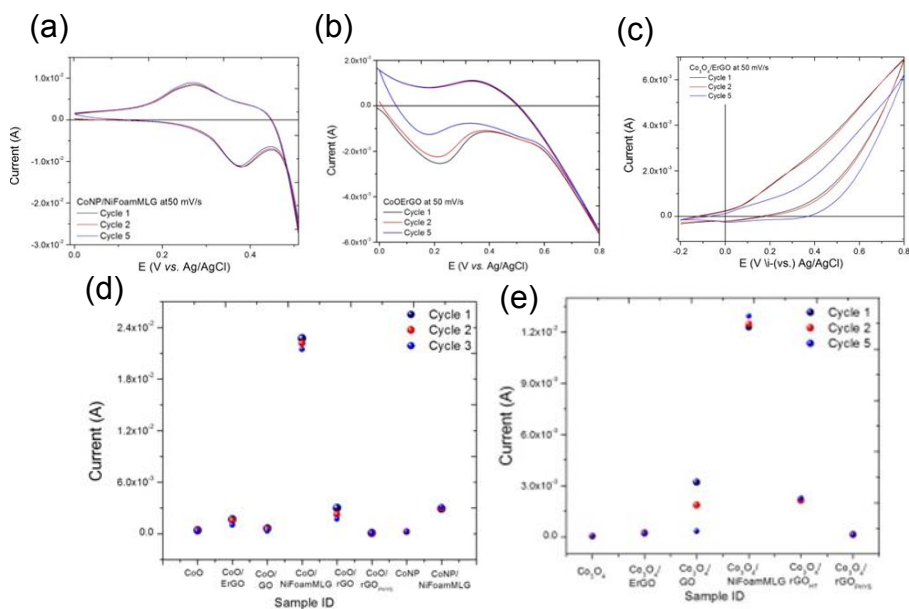
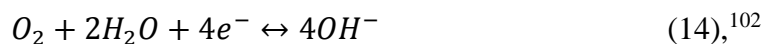


Figure 30. CV curves containing ORR catalysis assisted by representative samples: (a) CoNP/MLG, (b) CoO/ErGO, and (c) Co₃O₄/ErGO, with corresponding current response at 0.4 V for (d) CoO and (e) Co₃O₄ based hybrids.

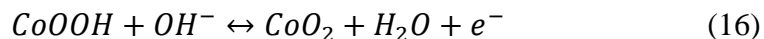
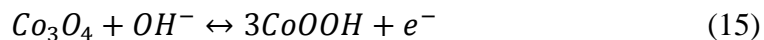
Co₃O₄/ErGO occurred at 0.2 V and 0.4 V, attributed to four-electron mechanism of ORR (0.401 V)



showing small variation/shifting between cycles (Fig. 30a-c) as observed in the previous CV. The current response indicative of the ability of the hybrids to reduce/oxidize oxygen was measured for all cycles at 0.2 V (Figs. 30c and 30d), having little to no variation among cycles for most hybrids and finding maximum values for CoO/MLG and Co₃O₄/MLG (2.1×10^{-2} A and 1.2×10^{-2} A, respectively). The performance for these hybrids could be attributed to the closely connected three-dimensional network formed by the foam that facilitates the flow of oxygen related species (H₂O and OH⁻) to the electrochemically active surface of the Co micro/nano crystallites for reduction/oxidation.

Even though commercial glucose sensors are available for purchase, they use enzymes as their mechanism of detection which raises their cost. In contrast, these affordable hybrids were able to detect glucose by means of electrochemical reduction/oxidation. While all hybrids have the potential to serve as sensor, we chose the composites that showed an outstanding electrochemical performance. These hybrids were monitored to observe their response to glucose in two experiments: using CV at 20 mV/s for various glucose concentrations (0.2 mM, 0.4 mM, 0.6 mM, 0.8 mM, and 1 mM) and using amperometry (0.45 V) for the progressive addition of 0.5 mL aliquots of 20 μ M glucose solution. An additional amperometric experiment was performed to explore the behavior of the hybrids towards glucose (0.1 M) addition while in the presence of other species (0.1 M uric acid-UA and 0.1 M ascorbic acid-AA) present in

the human body (Fig. 31). Figure 31a shows the CV curve for $\text{Co}_3\text{O}_4/\text{MLG}$ in which I and II correspond to redox pair



and III and IV correspond to redox pair



reducing/oxidizing glucose from/to gluconolactone (Fig. 32) which confirms the expected electroactive response of Co. The characteristic features of the redox peaks are accentuated for 0.6 mM glucose. Figure 31b shows the i - t plot for representative samples with highest current response for $\text{Co}_3\text{O}_4/\text{rGO}_{\text{HT}}$. The inconsistency of current value with respect to glucose addition could be attributed to experimental error during the stirring of the solution after addition. Similarly, Figure 31c shows the i - t plot for UA, AA, and glucose addition where all samples show a progression in which the current increases upon glucose addition, emphasizing the capability of the hybrid to detect glucose even in the presence of other substances.

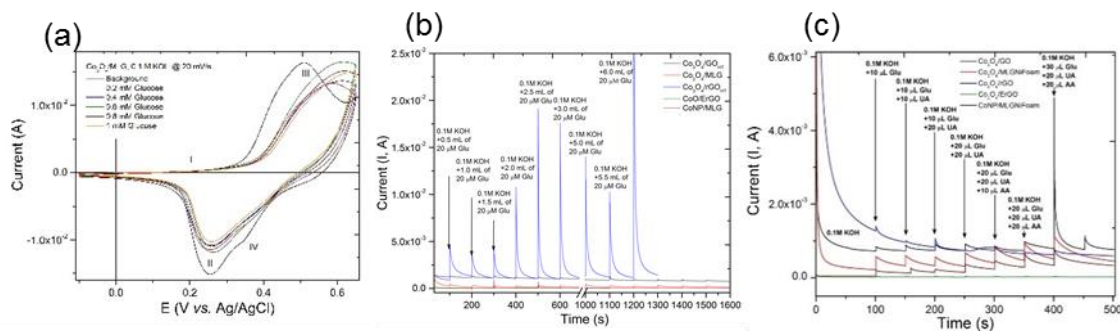


Figure 31. (a) cyclic voltammogram for $\text{Co}_3\text{O}_4/\text{MLG}$ in various glucose concentrations, current response (i - t plots) for chosen hybrids of (b) glucose alone and (c) glucose upon addition of uric acid and ascorbic acid.

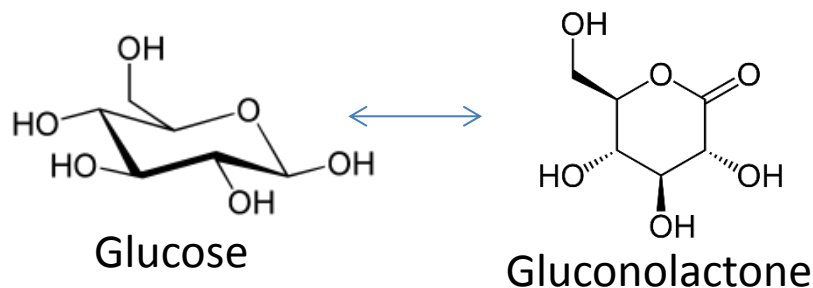


Figure 32. Depiction of the structure of glucose and its oxidized form gluconolactone

3.2 Conclusion

The results obtained through the different electrochemical techniques emphasized and confirmed the enhanced electrochemical performance of these hybrids as supercapacitor electrodes. From the different graphene based hybrids, $\text{Co}_3\text{O}_4/\text{rGO}_{\text{HT}}$, CoO/rGO , and CoO/MLG yielded high values of C_s , diffusion coefficient, and C_{if} and had some of the lowest charge-discharge time (0.46 s, 3.83 s, 0.83 s, respectively), indicating that hydrothermal synthesis and electrodeposition produces a synergistic blend of these two materials that allows high surface area and high density of electroactive sites for ion adsorption and electron transfer. In addition, stronger adherence of the material to the substrate was observed for electrodeposited and hydrothermally synthesized electrodes, highlighting their advantage as synthetic approaches as compared to physisorption. Particularly, the structural features of the graphene variants showed to strongly contribute to the performance. While for ErGO and rGO , the surface defects and functionalities act as both chemical linkage between the graphene support and the metal oxide and highly reactive sites, for MLG , the intertwined network from the Ni foam template permits accessibility for ion transport. Therefore, the combination of both the electrochemical properties and structural characteristics of both materials improves the performance of these electrodes as

supercapacitors. In addition, these hybrids showed potential as electrocatalytic platforms toward oxygen reduction reaction (namely CoO and Co₃O₄ on MLG), likely following the four-electron pathway, and toward glucose sensing with high current responses upon glucose addition alone and in the presence of other species.

Chapter 4: Summary and Future Prospects

As potential alternative sources of energy storage, cobalt oxide (s)/graphene hybrid electrodes were integrated by using physisorption, electrochemical anchoring, and hydrothermal synthesis. Their physical and electrochemical properties were collected to create a library of electroactive materials with potential application in electrocatalysis and glucose sensing. Even though all synthetic methods yielded successful coupling observed in the results from TEM and SEM (surface morphology), XRD (crystal structure), and Raman Spectroscopy (lattice vibrations), the electrochemical and hydrothermal synthesis showed outstanding electrochemical performance, suggesting enhancement of the synergy between Co and Gr likely owing to chemical binding rather than solely physical interaction. In fact, electrochemical properties including higher values of specific capacitance and low frequency capacitance along with fast charge-discharge time response and durability upon current cycling highlighted the potential for hybrids such as $\text{Co}_3\text{O}_4/\text{rGO}_{\text{HT}}$, CoO/rGO , CoO/ErGO and CoO/MLG as supercapacitive electrodes. Additional parameters, obtained through EIS modeling and SECM probe approach and imaging allowed further insight into the physical and chemical processes occurring at the interfacial boundary, emphasizing the hybrid nature of the electrodes and their highly electroactive surfaces. As the observed improvement of the electrochemical performance is directly related to the charge transfer dynamics with its corresponding physical and electronic structural modifications, in-situ Raman spectroscopy studies were employed, monitoring these changes as a function of applied bias. Even though the preliminary results shown here point towards charge transfer evidenced in cobalt peak position variation potentially

interrelated to changes in the position of G peak, more information can be extracted from this data to clearly establish the storage mechanisms and dynamics of electron/ion transport occurring at the interface. Additionally, theoretical approximations of the bonding and antibonding electronic structures of cobalt in the presence of graphene could provide a deeper understanding of the structural shifting occurring as a consequence of electron promotion between cobalt and graphene and its association with ion transport.

Appendix A: In-Situ Raman Spectroelectrochemistry of Graphene-based Hybrids

In this appendix, Raman spectroscopy and electrochemistry were coupled to monitor the spectral changes with applied potential to understand the physical and chemical processes occurring at the electrode-electrolyte interface. The preliminary results obtained using this integrated technique will provide insights into the charge transfer dynamics of the hybrids.

Experimental Setup

The measurements were performed in a customized three-electrode cell with a side opening for the sample, space for the silver chloride reference electrode and the platinum counter electrode. The electrolyte solution was lowered from previous ECHM experiments to 0.5 M KOH to avoid deterioration of the samples. Each hybrid was introduced into the sample slit and fixed with Teflon tape to prevent electrolyte leakage and was further mounted on a glass slide under the Raman microscope (Fig. A1). The Raman data was collected for each potential (from -0.2 V to 0.8 in increments of 0.1 V) to capture cobalt related peaks, D and G, and 2D in three separate sections ($300\text{-}800\text{ cm}^{-1}$, $1100\text{-}1800\text{ cm}^{-1}$, and $2450\text{-}2850\text{ cm}^{-1}$, respectively) with a 633 nm laser ($E_L = 1.92\text{ eV}$) at 100x magnification and 50% laser power. While the experiments were conducted, the *i-t* curves were observed to ensure the electrochemical stability of the system.

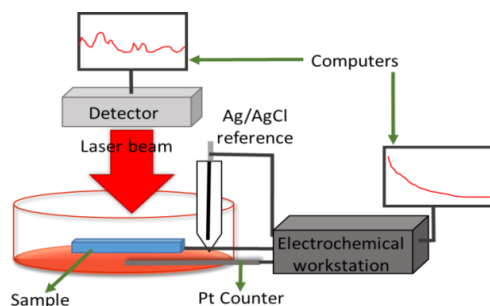


Figure A1. Sketch of the in-situ set up experiments.

Results and Discussion

The collected Raman spectra of major peaks (Co_{400} , Co_{600} , Co_{700} , $\text{D}\sim 1340\text{ cm}^{-1}$, $\text{G}\sim 1590\text{ cm}^{-1}$, $2\text{D}\sim 2680\text{ cm}^{-1}$) was obtained and plotted for a series of potentials as shown in representative example of $\text{Co}_3\text{O}_4/\text{ErGO}$ (Fig. A2). Despite the liquid medium and potential loss of intensity due to scattering, all characteristic bands were captured as previously found in air-acquired spectra. Shifting in wavenumber for D, G, and 2D peaks was observed likely associated with mechanical deformation for D and 2D and changes in the C-C bond length for G (Fig. A2b). At positive potentials (0 V-0.4 V), all peaks of interest are more distinct; however, decrease in intensity and loss of character (broadening) was identified at high potentials which could be attributed to different occupations of bonding and antibonding states for G peak in the case of C-C bonds and potentially for Co-C bonds and to electrostatic factors including the electric field generated by the applied potential.¹⁰³

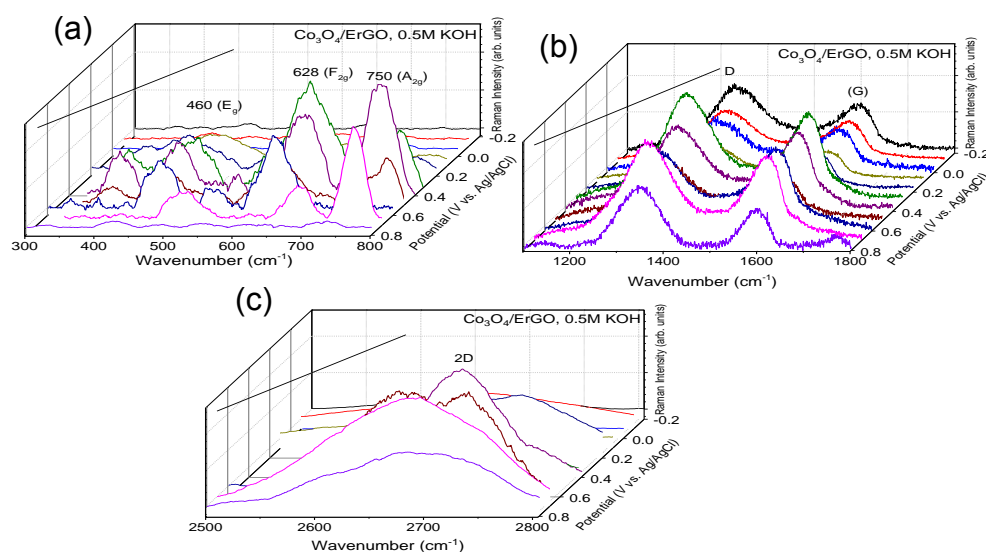


Figure A2. In-situ Raman spectra of $\text{Co}_3\text{O}_4/\text{ErGO}$ as a function of applied electrochemical biases, monitoring characteristic peaks, (a) Co bands, (b) D and G bands and (c) 2D band.

The band position of ω_{Co} , ω_D , ω_G , and ω_{2D} , intensity ratios of D to G (I_D/I_G), and 2D to G (I_{2D}/I_G) are plotted as a function of potential (Fig. A3). In Fig. A3a, an increasing trend is exclusively observed for ω_D corresponding to mechanical deformation, but in Figs. A3b-A3d, ω_{Co_pk2} , ω_G , and ω_{2D} follow a decreasing pattern from 0.2 V onwards. While the peak position of Co_{400} resembles the trend of ω_G , and ω_{2D} which may suggest no structural modification for those particular peaks (Co_{400} not engaging in charge transfer), the position of Co_{700} follows an opposite behavior to ω_D and ω_G which might be indicative of charge transfer occurring between the Co nanoparticles and the graphene, with Co being oxidized- Co_{700} increases and graphene being reduced, G peak decreases (Fig. A3e). I_D/I_G as a semi-quantitative measure of defect density shows apparent variation for positive applied potential. As seen in the rGO based hybrids synthesized from physisorption, ErGO decorated with Co_3O_4 seemed to adopt similar trend of n-type point defects for 0.2 V, 0.4 V, and 0.7 V, where G band increases and 2D band decreases. However, most of the potentials showed both a

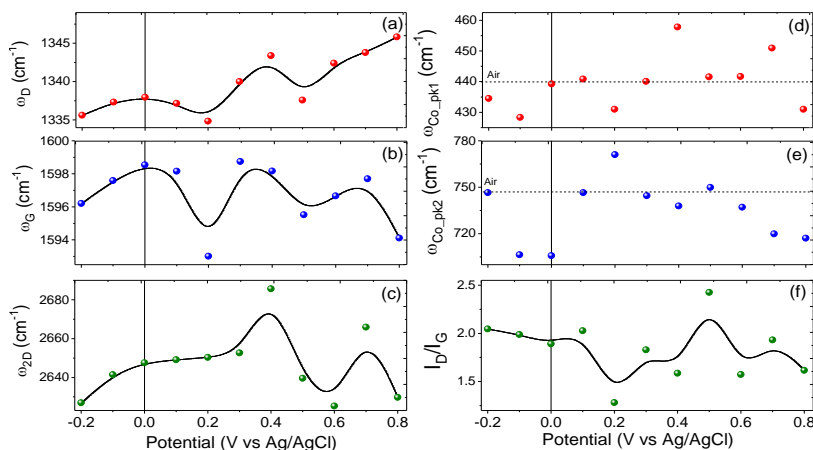


Figure A3. Variation of prominent Raman spectral bands for representative $Co_3O_4/ErGO$ hybrid in terms of (a) ω_D , (b) ω_G , (c) ω_{2D} , (d) ω_{COPk1} , (e) ω_{COPk2} , and (f) I_D/I_G .

combination of both p- and n- type where G band decreased and 2D band increased (p-type) or both bands increased (p-/n-type), demonstrating the dependency upon applied electrochemical bias.

Conclusion

The work of this chapter serves as a platform to investigate the charge transfer dynamics and mechanisms of the hybrids. Even though this information requires further analysis due to its novelty, the current spectroscopic data provided a semi-quantitative validation of the initial observations from previous Raman spectra and analysis (physically deposited hybrids) where charge transfer was predicted. Theoretical calculations may facilitate the interpretation of these data to gain more insight regarding the structural modifications that allow ion/electron transport between Co and graphene variants.

References

- ¹ Energy Sources, US Department of Energy, <https://energy.gov/science-innovation/energy-sources> (23 February, 2017).
- ² J. A. Turner, *Science* **285**, 687-689 (1999).
- ³ M. C. dos Santos, O. Kesler, and A. L. M. Reddy, *J. Nanomater.* **2012**, 1-2 (2012).
- ⁴ H. Ramsurn and R. B. Gupta, *ACS Sustain. Chem. Eng.* **1**, 779–797 (2013).
- ⁵ Q. Zhang, E. Uchaker, S. L. Candelaria, and G. Cao, *Chem Soc. Rev.* **42**, 3127-3171, (2013).
- ⁶ G. P. Kissling, D. O. Milesa, and D. J. Fermín, *Phys. Chem. Chem. Phys.* **13**, 21175–21185 (2011).
- ⁷ Q. Lu, J. G. Chen, and J. Q. Xiao, *Angew. Chem. Int. Ed.* **52**, 1882-1889 (2013).
- ⁸ *Handbook of Physics and Chemistry*, 67th Ed., **B-12**, CRC Press Inc. (1986-1987).
- ⁹ H.W. Kroto, J.R. Heath, S.C. O'Brian, R.F. Curl, and R.E. Smalley, *Nature* (London) **318**, 162 (1985).
- ¹⁰ H.W. Kroto, A.W. Allaf, and S.P. Balm, *Chem. Rev.* **91**, 1213-1235 (1991).
- ¹¹ Q.M. Zhang, Jae-Yel Yi, and J. Bernholc, *Phys. Rev. Lett.* **66**, 2633-2636 (1991).
- ¹² K. S. Novoselov, A. K. Geim, S. V. Morozov, D. Jiang, Y. Zhang, S. V. Dubonos, I. V. Grigorieva, and A. A. Firsov. *Science* **306**, 666-669 (2004).
- ¹³ S. Gupta and A. Irihamye, *Appl. Phys. Lett.* **5**, 1-14 (2015).
- ¹⁴ M. C. Lemme. *Solid-State Electron.* **52**, 514-518 (2008).
- ¹⁵ K. I. Bolotin, K.J. Sikes, Z. Jiang, M. Klima, G. Fudenberg, J. Hone, P. Kim, H. L. Stormer. *Solid State Commun.* **146**, 351-355 (2008).
- ¹⁶ C. Lee, X.D. Wei, J.W. Kysar, and J. Hone. *Science* **321**, 385-388 (2008).

-
- ¹⁷ M.D. Stoller, S. Park, Y. Zhu, J. An, and R.S. Ruoff. *Nano Lett.* **8**, 3498-3502 (2008).
- ¹⁸ R. Narayanan, H. Yamada, M. Karakaya, R. Podila, A. M. Rao, and P. R. Bandaru, *Nano Lett.* **15**, 3067-3072 (2015).
- ¹⁹ A. Bianco, H. M. Cheng, T. Enoki, Y. Gogotsi, R. H. Hurt, N. Koratkar, et al. *Carbon* **65**, 60-3 (2013).
- ²⁰ A. Ivanovskii, *Russ. Chem. Rev.* **81**, 751-605 (2012).
- ²¹ F. Perrozzi, S. Prezioso, L. J. Ottaviano, *J. Phys. Condens. Matter.* **27**, 1-21 (2015).
- ²² G. Eda and M. Chhowalla, *Adv. Mater.* **22**, 2392-2415 (2010).
- ²³ Y. Li, K. Sheng, W. Yuan, and G. Shi, *Chem. Commun.* **49**, 291-293 (2013).
- ²⁴ Y. Lu, Y. Jiang, W. Wei, H. Wu, M. Liu, L. Niu, W. J. Chen. *Mater Chem.* **22**, 2929-2934 (2012).
- ²⁵ C. Chung, Y-G. Kim, D. Shin, A-R. Ryoo, B. H. Hong, and D-H. Min. *Acc. Chem. Res.* **46**, 2211-2224 (2013).
- ²⁶ S. A. Grigor'ev, A. S. Pushkarev, V. N. Kalinichenko, I. V. Pushkareva, M. Y. Presnyakov, and V. N. Fateev, *Kinet. Catal.* **56**, 689-693 (2015).
- ²⁷ S. Junling, Z. Yin, Z. Yang, P. Amaladass, S. Wu, J. Y, Y. Zhao, W-Q. Deng, H. Zhang, and X. Liu. *Chem. Eur. J.* **17**, 10832-10837 (2011).
- ²⁸ M. Stoller, S. Park, Y. Zhu, J. An, and R. Ruoff, *Nano Lett.* **8**, 3498-3502 (2008).
- ²⁹ J. Hou, Y. Shao, M. W. Ellis, R. B. Moore, and B. Yi, *Phys. Chem. Chem. Phys.* **13**, 15384-15402 (2011).
- ³⁰ N. Ghaderi and M. J. Peressi. *Phys. Chem. C.* **114**, 21625-21630 (2010).
- ³¹ D. S. Sutar, G. Singh, and V. D. Botcha, *Appl. Phys. Lett.* **101**, 1-5 (2012).

-
- ³² S. Gupta and S. B. Carrizosa, *J. Electron. Mater.* **44**, 4492-4509 (2015).
- ³³ B. H. Min, D. W. Kim, K. H. Kim, H. O. Choi, S. W. Jang, and H-T. Jung. *Carbon* **80**, 446-452 (2014).
- ³⁴ Z-J. Lu, M-W. Xu, S-J. Bao, K. Tan, H. Chai, C-J. Cai, C-C. Ji, and Q. Zhang, *J. Mater. Sci.* **48**, 8101-8107 (2013).
- ³⁵ D. Friedman, T. Masciangioli, and S. O. Ison, "Critical Materials in Catalysis." *In The Role of the Chemical Sciences in Finding Alternatives to Critical Resources: A Workshop Summary*. The National Research Council (US) Chemical Sciences Roundtable. Press: Washington, D. C., (2012) pp. 13-21.
- ³⁶ Q. Guan, J. Cheng, X. Li, B. Wang, L. Huang, F. Nie and W. Ni, *Sci. Rep.* **5**, 1-10 (2015).
- ³⁷ Y. Liang, Y. Li, H. Wang, and H. Dai, *J. Am. Chem. Soc.* **135**, 2013-2036 (2013).
- ³⁸ J. Xiao, Q. Kuang, S. Yang, F. Xiao, S. Wang, and L. Guo, *Sci. Rep.* **3**, 1-8 (2013).
- ³⁹ R. B. Rakhi, W. Chen, D. Cha, and H. N. Alshareef, *Nano. Lett.* **12**, 2559-2567 (2012).
- ⁴⁰ V. F. Puentes, K. M. Krishnan, and A. P. Alivisatos, *Science* **291**, 2115-2117 (2001).
- ⁴¹ L. Wu, Q. Li, C. H. Wu, H. Zhu, A. Mendoza-Garcia, B. Shen, J. Guo, and S. J. Sun, *J. Am. Chem. Soc.* **137**, 7071-7074 (2015).
- ⁴² Y. A. Kozinkin, V. V. Pryadchenko, and L. A. Bugaev, *Bull. Russ. Acad. Sci., Phys.* **75**, 1674-1675 (2011).
- ⁴³ D. Gu, C-J. Jia, C. Weidenthaler, H-J. Bongard, B. Spliethoff, W. Schimdt, and F. J. Schüth, *J. Am. Chem. Soc.* **137**, 11407-11418 (2015).

-
- ⁴⁴ L. J. Suchow, *J. Chem. Educ.* **53**, 560 (1976).
- ⁴⁵ V. R. Shinde, S. B. Mahadik, T. P. Gujar, and C. D. Lockhande, *App. Surf. Sci.* **252**, 7487-7492, (2006).
- ⁴⁶ D. Zhao, Y. Wang, and Y. Zhang, *Nano-Micro Lett.* **3**, 62-71 (2011).
- ⁴⁷ S. R. C. Vivekchand, C. S. Rout, K. S. Subrahmanyam, A. Govindaraj, and C. N. R. Rao, *J. Chem. Sci.* **120**, 9–13 (2008)
- ⁴⁸ A. J. Bard, and L. R. Faulkner, *Electrochemical Methods: Fundamentals and Applications*, 2nd Ed., John Wiley & Sons, Inc. (2001) pp. 1-44, 368-405, 534-570, 662-670.
- ⁴⁹ S. Roldan, D. Barreda, M. Granda, R. Menendez, R. Santamaria, and C. Blanco, *Phys. Chem. Chem. Phys.* **17**, 1084-1092 (2015).
- ⁵⁰ B. E. Conway, *J. Electrochem. Soc.* **138**, 1539-1548 (1991).
- ⁵¹ J. M. Tarascon and M. Armand, *Nature* **414**, 358-367 (2001).
- ⁵² Y. Yang, Z. Peng, G. Wang, G. Ruan, X. Fan, L. Li, H. Fei, R. H. Hauge, and J. M. Tour, *ACS Nano* **8**, 7279-7287 (2014).
- ⁵³ A. J. Appleby, *Catal. Rev.* **4**, 221-244 (1970).
- ⁵⁴ Adapted from <https://energy.gov/eere/fuelcells/types-fuel-cells>
- ⁵⁵ Z. Zhu, L. Garcia-Gancedo, A. J. Flewitt, H. Xie, F. Moussy, and W. I. Milne, *Sensors* **12**, 5996-6022 (2012).
- ⁵⁶ J. I. Goldstein, D. E. Newbury, P. E. Echlin, D. C. Joy, C. Fiori, and E. Lifshin. *Scanning Electron Microscopy and X-Ray Microanalysis. A Text for Biologists, Material Scientists, and Geologists*. Plenum, New York (1981) pp. 21-68, 273-339.

-
- ⁵⁷ S. L. Flegler, J. W. Heckman, Jr., and K. L. Klomparens, *Scanning and Transmission Electron Microscopy: An Introduction*. Oxford University Press, New York. **43** (1993) pp. 43-48, 173-196.
- ⁵⁸ B. D Cullity. *Elements of X-ray diffraction*. 2nd Ed. Addison-Wesley, Reading, Mass. (1978) pp. 259-320.
- ⁵⁹ D. A. Long, *Raman Spectroscopy*. McGraw-Hill. (1977) pp. 157-165.
- ⁶⁰ P. T. Kissinger and W. R. Heineman, *J. Chem. Educ.* **60**, 702-706 (1983).
- ⁶¹ E. Barsoukov and J. R. MacDonald, *Impedance Spectroscopy: Theory, Experimental, and Applications*. 2nd Ed. John Wiley & Sons, Inc. (2005) pp. 469-497.
- ⁶² A. Salimi and R. Hallaj, *J. Solid State Electrochem.* **16**, 1239-1246 (2012).
- ⁶³ “Testing Electrochemical Capacitors Part 2: Cyclic-Charge and Discharge and Stacks.” *Application Note Rev. 2*. Gamry Instruments, Inc. (2015).
- ⁶⁴ W. Hummers and R. J. Offeman, *J. Am. Chem. Soc.* **80**, 1339-1339 (1958).
- ⁶⁵ S. Park, J. An, R. J. Potts, A. Velamakanni, S. Murali, and R. S. Ruoff, *Carbon* **49**, 3019-3023 (2011).
- ⁶⁶ D. C. Marcano, D. V. Kosynkin, J. M. Berlin, A. Sinitskii, Z. Sun, A. Slesarev, L. B. Alemany, W. Lu, and J. M. Tour, *ACS Nano*. **4**, 4806-4814 (2010).
- ⁶⁷ W. S. Hummers and R. E. Offeman, *J. Am. Chem. Soc.* **80**, 1339–1339 (1958).
- ⁶⁸ S. Gupta, S. B. Carrizosa, B. McDonald, J. Jasinski, and N. Dimakis, *J. Mater. Res.* **32**, 301-322 (2017).
- ⁶⁹ M. Ding, Y. Tang, and A. Star, *J. Phys. Chem. Lett.* **4**, 147-160 (2013).
- ⁷⁰ S. Gupta, E. Heintzman, and J. Jasinski, *J. Electron. Mater.* **43**, 3458-3469 (2014).

-
- ⁷¹ S. Greenwald, *Acta Crystallogr.* **6**, 396-398 (1953).
- ⁷² W. L. Smith and A.D. Hobson, *Acta Crystallogr.* **B29**, 362-363 (1953).
- ⁷³ H. M. Rietveld, *J. Appl. Cryst.* **2**, 65-71 (1969).
- ⁷⁴ O. Zhou, R. M. Fleming, D. W. Murphy, C. H. Chen, R. C. Haddon, and A. P. Ramirez, *Science* **263**, 1744-1747 (1994).
- ⁷⁵ U. Holzwarth and N. Gibson, *Nature Technology* **6**, 534 (2011).
- ⁷⁶ A. C. Ferrari, *Solid State Commun.* **143**, 47-57 (2007).
- ⁷⁷ V. G. Hadjiev, M. N. Iliev, and I. V. Vergilov, *J. Phys. C: Solid State Phys.* **21**, 1199 (1988).
- ⁷⁸ W. I. Roth, *J. Phys. Chem. Solids* **25**, 1-10 (1964).
- ⁷⁹ H. Shirai, Y. Morioka, and I. Nakagawa, *J. Phys. Soc. Japan* **51**, 592-597 (1982).
- ⁸⁰ H. Poulet and J. P. Mathieu, *Spectres de Vibration et Symetrie de Cristaux*, Paris: Gordon and Breach. (1970) pp. 23-45.
- ⁸¹ F. Albert Cotton, *Chemical Applications of Group Theory*, 3rd Ed. John Wiley & Sons Inc. (1990) pp. 204-251, 304-346.
- ⁸² J. R. Ferraro and K. Nakamoto, *Introductory Raman spectroscopy*. Boston: Academic Press (1994) pp. 29-78.
- ⁸³ I. Rusakova, T. O. Ely, C. Hofmann, D. P.-Centurion, C. S. Levin, N. J. Halas, A. Luttge, and K. H. Whitmire, *Chem. Mater.* **19**, 1369-1375 (2007).
- ⁸⁴ C. M. Julien and M. Massot, *J. Phys. Condens. Matter* **15**, 3151-3162 (2003).
- ⁸⁵ L. G. Cançado, K. Takai, T. Enoki, M. Endo, Y.A. Kim, H. Mizusaki, A. Jorio, L.N. Coelho, R. Magalhaes-Paniago, and M.A. Pimenta, *Appl. Phys. Lett.* **88**, 1-3 (2006).

-
- ⁸⁶ K. Sato, R. Saito, Y. Oyama, J. Jiang, L.G. Cancado, M.A. Pimenta, A. Jorio, G. Ge. Samsonidze, G. Dresselhaus, and M.S. Dresselhaus, *Chem. Phys. Lett.* **427**, 117-121 (2006).
- ⁸⁷ J. S. Park, A. Reina, R. Saito, J. Kong, G. Dresselhaus, and M.S. Dresselhaus, *Carbon* **47**, 1303-1310 (2009).
- ⁸⁸ M. W. Iqbal, A. K. Singh, M. Z. Iqbal, and J. Eom, *J. Phys. Condens. Matter* **24**, 1-7 (2012).
- ⁸⁹ X. W. Xie, Y. Li, and Z.Q. Liu, *Nature* **458**, 746-749 (2009).
- ⁹⁰ L. H. Hu, Q. Peng, and Y.D. Li, *J. Am. Chem. Soc.* **130**, 16136-16137 (2008).
- ⁹¹ L. Hu, K. Sun, Q. Peng, B. Xu, and Y. Li, *Nano Res.* **3**, 363-368 (2010).
- ⁹² J. Jansson, *J. Catal.* **194**, 55-60 (2000).
- ⁹³ P. Broqvist, I. Panas, and H. Persson, *J. Catal.* **210**, 198-206 (2002).
- ⁹⁴ M. C. Toroker, D. A. Kanan, N. Alidoust, L. Y. Isseroff, P. Liao, and E. A. Carter, *Phys. Chem. Chem. Phys.* **13**, 16644-16654 (2011).
- ⁹⁵ F. Grillo, M.M. Natile, and B. Glisenti, *Appl. Catal. B-Environ.* **48**, 267-274 (2004).
- ⁹⁶ V.V. Ilyasov, D. A. Velikokhatskii, I. V. Ershov, I. Y. Nikiforov, and T. P. Zhdanova, *J. Struct. Chem.* **52**, 849-860 (2011).
- ⁹⁷ V.V. Ilyasov, D. A. Velikokhatskii, I. V. Ershov, I. Y. Nikiforov, and T. P. Zhdanova, *J. Mod. Phys.* **2**, 1120-1135 (2011).
- ⁹⁸ S. H. Huh, *Carbon* **78**, 617-621 (2014).
- ⁹⁹ I. Childres, L. A. Jaureguib, W. Parkb, H. Caoa, and Y. P. Chena. (2010) pp. 1-20.

¹⁰⁰ L. Wang, G. Duan, J. Zhu, S-M. Chen, X-H. Liu, and S. Palanisamy. *J. Colloid Interface Sci.* **483**, 73–83 (2016).

¹⁰¹ Z-C. Yang, C-H. Tang, Y. Zhang, H. Gong, X. Li, and J. Wang, *Sci. Rep.* **3**, 1-7 (2013).

¹⁰² J. Zhang, Z. Xia, and L. Dai, *Sci. Adv.* **1**, 1-20 (2015).

¹⁰³ S. Gupta and J. Robertson, *J. Appl. Phys.* **100**, 1-9 (2006).